

# The AAO/UKST SuperCOSMOS H $\alpha$ Survey (SHS)

Q.A. Parker<sup>1,3</sup>, S. Phillipps<sup>2</sup>, M.J. Pierce<sup>2</sup>, M. Hartley<sup>4</sup>, N.C. Hambly<sup>5</sup>, M.A. Read<sup>5</sup>,  
H.T. MacGillivray<sup>5</sup>, S.B. Tritton<sup>5</sup>, C.P. Cass<sup>4</sup>, R.D. Cannon<sup>3</sup>, M. Cohen<sup>6</sup>, J.E. Drew<sup>7</sup>,  
D.J. Frew<sup>1</sup>, E. Hopewell<sup>7</sup>, S. Mader<sup>8</sup>, D.F. Malin<sup>3</sup>, M.R.W. Masheder<sup>2</sup>, D.H. Morgan<sup>5</sup>,  
R.A.H. Morris<sup>2</sup>, D. Russeil<sup>9</sup>, K.S. Russell<sup>4</sup>, R.N.F. Walker<sup>2</sup>

<sup>1</sup> *Macquarie University, Sydney, Australia,*

<sup>2</sup> *Astrophysics Group, University of Bristol, Tyndall Avenue, Bristol, U.K.*

<sup>3</sup> *Anglo-Australian Observatory, Epping, New South Wales, Australia*

<sup>4</sup> *UK Schmidt Telescope, Anglo-Australian Observatory, Siding Spring, New South Wales, Australia*

<sup>5</sup> *Institute for Astronomy, School of Physics, University of Edinburgh,* <sup>6</sup> *UC, Berkeley, USA*

<sup>7</sup> *Imperial College, London, U.K.*

<sup>8</sup> *Australia Telescope National Facility, Parkes, Australia,*

<sup>9</sup> *Observatoire de Marseille, 2 Place le Verrier, Marseille, 13248 cedex 4, France*

Accepted . Received ; in original form

## ABSTRACT

The UK Schmidt Telescope (UKST) of the Anglo-Australian Observatory completed a narrow-band H $\alpha$  plus [NII] 6548, 6584Å survey of the Southern Galactic Plane and Magellanic Clouds in late 2003. The survey, which was the last UKST wide-field photographic survey, and the only one undertaken in a narrow band, is now an on-line digital data product of the Wide-Field Astronomy Unit of the Royal Observatory Edinburgh (ROE). The survey utilised a high specification, monolithic H $\alpha$  interference band-pass filter of exceptional quality. In conjunction with the fine grained Tech-Pan film as a detector it has produced a survey with a powerful combination of area coverage (4000 square degrees), resolution ( $\sim 1$  arcsecond) and sensitivity ( $\leq 5$  Rayleighs), reaching a depth for continuum point sources of  $R \simeq 20.5$ . The main survey consists of 233 individual fields on a grid of centres separated by  $4^\circ$  at declinations below  $+2^\circ$  and covers a swathe approximately  $20^\circ$  wide about the Southern Galactic Plane. The original survey films were scanned by the SuperCOSMOS measuring machine at the Royal Observatory, Edinburgh to provide the on-line digital atlas called the SuperCOSMOS H $\alpha$  Survey (SHS). We present the background to the survey, the key survey characteristics, details and examples of the data product, calibration process, comparison with other surveys and a brief description of its potential for scientific

## 1 INTRODUCTION

H $\alpha$  emission from HII regions is one of the most direct optical tracers of current star formation activity and is routinely used to measure star formation rates in external galaxies (e.g. Kennicutt 1992). In our own galaxy, HII regions are seen by direct UV illumination of molecular clouds from adjacent hot stars and as highly structured shells, bubbles and sheets of emission resulting from supernovae, planetary nebula, Wolf-Rayet stars and other stellar outflows. Some large-scale outflows can, in turn, be themselves a trigger of star formation, and their morphology is strongly influenced by the nature and density of the ISM into which they expand. H $\alpha$  imaging allows this to be studied in great detail in our immediate Galactic neighbourhood and to be detected at a great distance in external galaxies. The UV flux from hot stars also excites a more diffuse emission from the ISM, unconnected to current star formation and detectable over large areas of sky.

The perimeters of some large emission shells appear to enclose the locations of more recent star formation which may in turn generate further supernovae and stellar winds (Dopita, Matthewson & Ford 1985), while their morphology informs the processes by which star formation is propagated (e.g. Elmegreen & Lada 1977, Gerola & Seiden 1978). Because of proximity, some of these structures can present very large angular sizes such as Barnard's loop (probably the first large-scale emission structure detected in the Galaxy) which subtends  $13^\circ$  (Pickering 1890) and the Gum nebula which at  $36^\circ$ , is even larger (Gum 1952). More distant complexes or groups of HII regions, such as NGC 6334, can still be of the order  $1^\circ$  across and yet present fine detail on arcsecond scales (Meaburn & White 1982). Given their interaction with their external large-scale environment (Tenorio-Tagle & Palous 1987) it was clear that emission-line imaging of these structures required an efficient wide-field capability and high spatial resolution.

On smaller scales, stellar H $\alpha$  emission characterises the short lived, least well understood stages of stellar evolution,

i.e. those of pre- and post-main sequence stars, planetary nebulae and close binary systems. Previous efforts to detect emission sources have either offered modest area coverage; e.g. the UBVI and H $\alpha$  photometric surveys of Sung, Chun & Bessell (2000) or Keller et al. (2001) or, where a large-area survey has been conducted, becomes incomplete at relatively bright magnitudes. An example is the objective-prism survey of Stephenson & Sanduleak (1977) which reaches only  $\sim 14^{\text{th}}$  magnitude. Such surveys are highly incomplete so their emission source catalogues provide only limited samples upon which to build our understanding of these rarely observed phases of stellar evolution.

From the above, the importance of Galactic H $\alpha$  line emission from both stars and nebulae is evident and this has encouraged many surveys for HII regions in particular, e.g. Sharpless (1953, 1959), Gum (1955), Hase & Shajn (1955), Bok, Bester & Wade (1955), Johnson (1955, 1956), Rodgers, Campbell & Whiteoak (1960), Georgelin & Georgelin (1970) and Sivan (1974). These earlier surveys were limited to relatively small targeted areas or had such wide fields of view that small-scale detail was lost due to the low angular resolution; e.g. the survey of Sivan (1974) used  $60^\circ$  field diameters giving a plate scale of  $\sim 6^\circ \text{ mm}^{-1}$ . Relatively little optical emission-line survey work had been done in a way that combined wide-angle coverage with good sensitivity and high resolution. These characteristics are essential to allow thorough examination of the morphology and interaction of emission regions with their environment on arcsecond to degree scales and to detect the large variety of stellar emission sources to suitably faint levels.

Hence, in the mid-1990s, a number of the present authors suggested that the U.K. Schmidt Telescope (UKST) should be used to make a narrow band photographic H $\alpha$  survey of the Southern Milky Way and Magellanic Clouds. The only previous wide-area UKST H $\alpha$  material comes from the work by Meaburn and co-workers in the 1970s (see Davies, Elliot & Meaburn 1976; Meaburn 1980). They used a  $100\text{\AA}$  band-pass multi-element mosaic filter and fast, but coarse grained, 098-04 emulsion. It covered some limited ar-

eas close to the Galactic Plane (Meaburn & White 1982), but was mainly influential in the study of the ionised gas in the Magellanic Clouds, showing the first evidence for “supergiant-shells” and other large-scale features (Davies et al. 1976, Meaburn 1980). There are other recent wide-area H $\alpha$  surveys such as that by the Virginia group in the northern hemisphere (VTSS – Dennison et al. 1998) and the Mount Stromlo group in the south (Buxton et al. 1998). Recently, Gaustad et al. (2001) have released the full “Southern H $\alpha$  Sky Survey Atlas” (SHASSA), covering the entire southern sky. This imaging survey has rather coarse, 48-arcsecond pixels and strong artefacts from uncanceled stars in the continuum-subtracted product, but has the major benefit of being directly calibrated in Rayleighs. These surveys continue the tradition of deep, low spatial resolution studies, but use CCDs which permit low flux densities of a few tenths of a Rayleigh to be achieved.

An alternative approach, taken by the Marseille and Wisconsin Fabry-Perot groups in the southern and northern skies respectively (see Russeil et al. 1997, 1998 and Haffner et al. 2003 for the WHAM – Wisconsin H $\alpha$  Mapper), was to obtain high resolution spectral (i.e. velocity) data, but again with low spatial resolution (e.g. 1 $^\circ$  pixels for WHAM).

A critical comparison between the WHAM, SHASSA and VTSS surveys was undertaken by Finkbeiner (2003) who presented a ‘whole-sky’ H $\alpha$  map. Significantly, none of these major surveys offer the arcsecond spatial resolution of the AAO/UKST H $\alpha$  survey. A summary of fundamental properties of these modern surveys is given in Table 1.

## 2 THE AAO/UKST H $\alpha$ SURVEY

The AAO/UKST H $\alpha$  survey provides a 5 Rayleigh sensitivity narrow-band survey of Galactic emission (H $\alpha$  plus [NII] 6548, 6584 $\text{\AA}$ ) with arcsecond spatial resolution. Henceforth the survey will be referred to simply as the H $\alpha$  survey though it is understood that this includes any [NII] emission component that is sampled by the filter band-pass (such emission can completely dominate H $\alpha$  for some PN types for

example). Approximately 4000 deg $^2$  of the Southern Milky Way have been covered to  $|b| \sim 10 - 13^\circ$  together with a separate contiguous region of 700 deg $^2$  in and around the Magellanic Clouds. Matching 3-hour H $\alpha$  and 15-min broad-band (5900-6900 $\text{\AA}$ ) short red (SR) exposures were taken over the 233 distinct but overlapping fields of the Galactic Plane and 40 fields of the Magellanic Clouds. These were done on 4 $^\circ$  centres because of the circular aperture of the H $\alpha$  interference filter which has a dielectric coating diameter of about 305mm ( $\sim 5.7^\circ$ ) deposited on a standard 356  $\times$  356mm red glass (RG610) substrate (refer Section 5). The overlapping 4 $^\circ$  field centres enable full, contiguous coverage in H $\alpha$  despite the circular filter aperture. Because of the slightly smaller effective field, a new Southern sky-grid of 1111, 4 $^\circ$  field centres was created (whose numbers should not be confused with the 893 standard 5 $^\circ$  field centres of the UKST Southern Sky Surveys). A map of the survey region in a standard UKST RA/DEC plot together with the new field numbers is available on the SHS web site<sup>1</sup>. In the on-line UKST plate catalogue these fields have a ‘h’ prefix (e.g. h123) to avoid confusion with the ESO/SERC 5 $^\circ$  fields.

The survey began in 1997 and took six years to complete. This latest and final UKST photographic survey was the first large-scale, narrow band survey undertaken on the telescope and is the first where the sole method of dissemination to the community is via access to on-line digital data products. Preliminary survey details and results were given by Parker & Phillipps (1998, 2003). The present paper is intended as the definitive reference for the survey. We describe the key characteristics of the survey, the on-line data product, some survey limitations, a flux calibration scheme, comparisons with other surveys and a brief overview of the potential for current and future scientific exploitation.

The arcsecond resolution of the AAO/UKST H $\alpha$  survey makes it a particularly powerful tool, not only for investigating the detailed morphology of emission features across the widest range of angular scales, but also as a means of

<sup>1</sup> <http://www-wfau.roe.ac.uk/sss/halpha/>

**Table 1.** Summary details of various current H $\alpha$  surveys

Survey	Coverage (sq.deg)	Depth Rayleighs	Resolution (arcsec)	Field size (degrees)	Filter FWHM	Coverage	Reference
WHAM <sup>1</sup>	17000	0.15	3600	1	0.25Å	$\delta > -30^\circ$	Haffner et al. 2003
SHASSA <sup>2</sup>	17000	$\sim 2$	48	13 $\times$ 13	32Å	$\delta < 15^\circ$	Gaustad et al. 2001
VTSS <sup>3</sup>	>1000	$\sim 2$	96	10 $\times$ 10	17Å	$\delta > -20^\circ$ (if completed)	Dennison et al. 1998
SHS <sup>4</sup>	4000	$\leq 5$	1-2	5.5 $\times$ 5.5	80Å	$\delta > +2^\circ$ ; $ b  \leq 10 - 13^\circ$	This paper
IPHAS <sup>5</sup>	1800	$\sim 3$	$\sim 1$	0.3 $\times$ 0.3	95Å	$ b  \leq 5^\circ$ ; northern plane	Drew et al. 2005

Note: 1 Rayleigh =  $10^6/4\pi$  photons  $\text{cm}^{-2} \text{s}^{-1} \text{sr}^{-1} = 2.41 \times 10^{-7}$  erg  $\text{cm}^{-2} \text{s}^{-1} \text{sr}^{-1}$  at H $\alpha$

<sup>1</sup>: <http://www.astro.wisc.edu/wham>; <sup>2</sup>: <http://amundsen.swarthmore.edu/SHASSA>;

<sup>3</sup>: <http://www.phys.vt.edu/~halpha>; <sup>4</sup>: <http://www-wfau.roe.ac.uk/ss/halpha/>

<sup>5</sup>: <http://astro.ic.ac.uk/Research/Halpha/North/>

identifying large numbers of faint point-source H $\alpha$  emitters, which include cataclysmic variables, T Tauri, Be and symbiotic stars, compact Herbig-Haro objects and unresolved planetary nebulae (PNe). Given the coincidence of the broad CIV/HeII blend in late-type Wolf Rayet stars, these objects can also be detected. Most other comparative surveys (Table 1) are largely insensitive to point-source emitters as they lack spatial resolution, being optimised instead for the faintest levels of resolved and diffuse emission.

On larger scales, the detailed spatial structure of the ionized ISM component traced by the new AAO/UKST H $\alpha$  survey can provide key data for many studies, e.g. mapping of specific areas for detailed spectroscopic follow-up to obtain emission-line gas kinematics or for dynamical studies of star forming regions, with their implications for the energetics of the central stars. Furthermore, comparisons with other indicators of star formation from other wavebands should provide essential clues to the active mechanisms. The survey also complements the recent Galactic Plane radio maps from MOST (Green et al. 1999), the new NIR maps from 2MASS (Jarrett et al. 2000) and the mid-infrared maps from the MSX satellite (Price et al. 2001).

Figure 1 presents two panels showing the 233 survey fields (mosaiced together by M.Read) to illustrate the overall survey coverage. The entire survey has been incorporated into an on-line mosaic within the freeware ‘Zoomify’ environment (see <http://www.zoomify.com>) which enables preliminary survey visualisation and scanning. The lowest resolution map can be zoomed-in to a level where each pixel repre-

sents about 12 arcseconds. This interactive map is available on-line.<sup>2</sup> This map is a factor of 18 lower in resolution than the full 0.67 arcsecond pixel survey data available on-line which should be used for serious scientific work. The success of this survey has led directly to a northern counterpart, currently underway on the 2.5m Isaac Newton Telescope on La Palma using a wide-field CCD camera and H $\alpha$  R and I band imaging; the Isaac Newton telescope Photometric H $\alpha$  Survey (IPHAS). This important survey is the subject of a separate paper (Drew et al. 2005) though a brief comparison in an overlap region is included later in Section 12.

### 3 THE DETECTOR: TECHNICAL PANCHROMATIC FILM-BASED EMULSION

The survey was carried out using Kodak Technical Panchromatic (Tech-Pan) Estar based films (e.g. Kodak 1987). The superb qualities of this emulsion and its adaptation for UKST use has been described in detail by Parker & Malin (1999) so only a very brief summary is given here. The Tech-Pan emulsion has remarkably high quantum efficiency for a photographic material with hypersensitised films having a DQE approaching 10 per cent (Phillipps & Parker 1993). Due to its original development in connection with solar patrol work, it has particularly high efficiency around H $\alpha$ . The Tech-Pan films are also extremely fine grained, with an inherent resolution of  $\sim 5\mu\text{m}$ , leading to an excel-

<sup>2</sup> <http://surveys.roe.ac.uk/ssa/hablock/hafull.html>

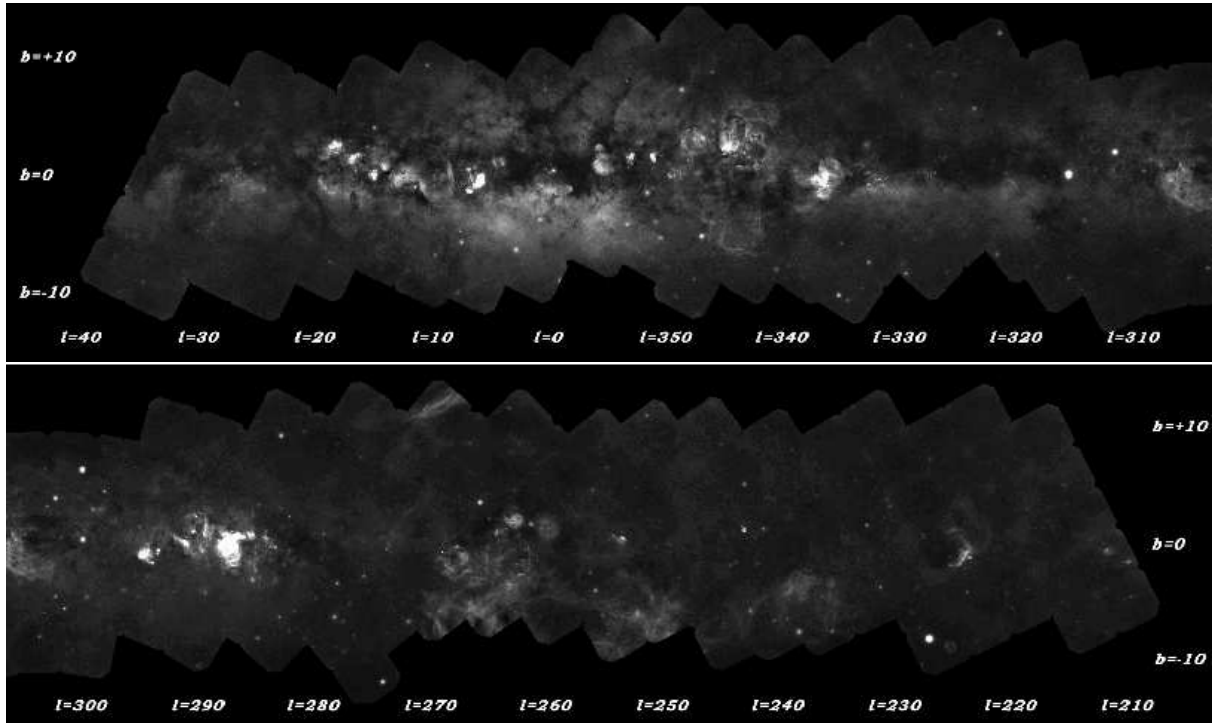


**Figure 1.** All 233 survey fields mosaiced together by M.Read: Top panel cover galactic longitude  $l=40$  to  $310$  degrees, bottom panel  $l=300$  to  $210$  degrees.

lent high-resolution imaging capability and a depth for point sources that exceeded that achieved for the more widely used glass-based IIIa-F emulsion by about a magnitude for standard UKST R-band survey 1-hour exposures (e.g. Parker & Malin 1999). These factors, combined with the wide area coverage available to Schmidt photographic surveys, made Tech-Pan an ideal choice for the Southern Galactic Plane  $H\alpha$  survey. The colour term stability of Tech-Pan compared to the IIIa- emulsions used at the UKST is given by Morgan & Parker (2005) where these terms are shown to be stable, reproducible, generally small, and similar to those previously derived for the older IIIa- emulsions. This gives confidence in the survey's photometric integrity. Over the survey life-time, photography on a Schmidt telescope still offered several advantages over CCD images, especially low cost and very fine spatial resolution and uniformity across a large physical area ( $356 \times 356$  mm) giving a  $40 \text{ deg}^2$  wide field of view. However, a key limitation is that the detector response is linear over only a narrow dynamic range so recovering and calibrating the intensity information needs careful treatment (see Section 11). In Figure 2 we present

small,  $3 \times 3$  arcminute regions to demonstrate the qualitative difference between the 3-hour  $H\alpha$  and 15-min SR Tech-Pan exposures and the standard 60-min R-band IIIa-F UKST survey data. This region includes a newly discovered planetary nebula (PHR1706-3544) found from the  $H\alpha$  survey data as part of the Macquarie/AAO/Strasbourg  $H\alpha$  planetary nebulae catalogue (Parker et al. 2003 and 2005 in preparation). Note the improved resolution of the Tech-Pan image, the very similar depth of the respective exposures for point sources and the tighter point-spread function (psf) for the Tech-Pan compared to the IIIa-F emulsion.

#### 4 THE NARROW BAND $H\alpha$ BAND-PASS FILTER

To take advantage of UKST's large field of view it was necessary to obtain a physically large narrow band-pass filter to be placed as close as possible to the telescope's focal plane. The issues involved with mounting such filters with Schmidt telescopes has been described by Meaburn (1978) and previous large interference filters were generally of the mosaic

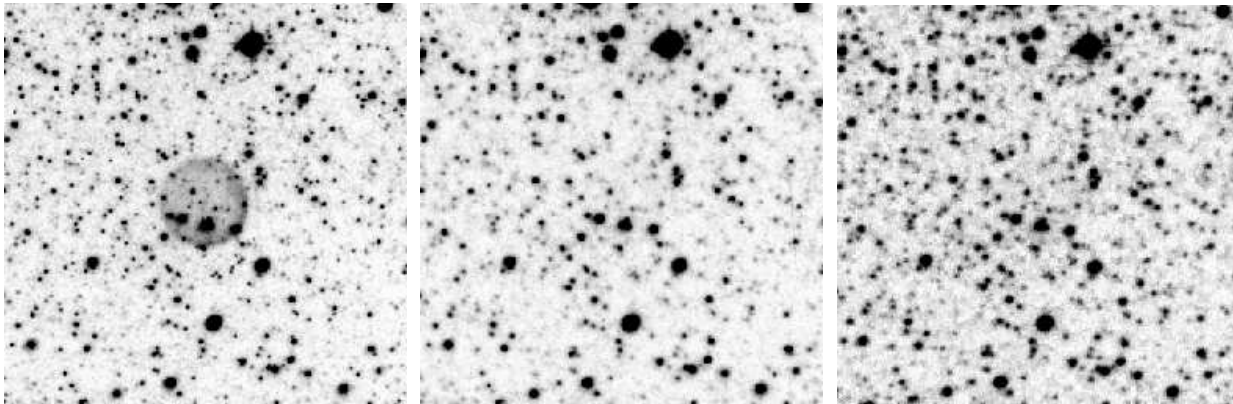


**Figure 2.**  $3 \times 3$  arcminute extracts of SuperCOSMOS data around a newly discovered PN (PHR1706-3544) from the 3-hour  $H\alpha$  survey data (a - left), matching 15 minute Tech-Pan SR data (b - middle) and earlier epoch 60 minute IIIa-F R-band data (c - right). The new PN is only visible in the  $H\alpha$  image. Note the well matched depth for point sources between all three exposures and the improved resolution of the Tech-Pan images compared with the IIIa-F exposure.

type (e.g. Meaburn 1980). Such smaller scale interference filters are easier to manufacture and can be made to higher optical quality. However, difficulties associated with their mounting often lead to problems of missing data in the filter gaps, degraded, variable resolution and lack of homogeneity over large survey areas, even when the optical quality of the elements themselves are excellent. This was the case for the Meaburn mosaic filters which did not fully deliver the anticipated performance due to an unfortunate index mis-match in optical cement between the components which resulted in reflection ghosts (which can be got rid of numerically after scanning), coupled with the practical difficulty of mounting the components in a sandwich to eliminate optical path variations (Meaburn, private communication).

Fortunately, it proved possible for the AAO to obtain a custom-made, exceptionally large, monolithic, thin-film interference filter from Barr Associates in the USA which avoids the problems that can be associated with mosaic filters. Detailed filter specifications and characteristics are given by Parker & Bland-Hawthorn (1998). The essential features are reviewed here for completeness together with some additional modeling of the filter profile in the converging beam when off-axis (see Pierce 2005 for further details). An RG610 glass substrate was cut to  $356 \times 356$ mm ( $\sim 6.5^\circ$ ), the standard size of UKST filters and coated with a multi-layer, dielectric stack to give a 3-cavity design with a clear

aperture of  $\sim 305$  mm diameter and with an effective refractive index of the equivalent monolayer of 1.34. This circular aperture of layered coating constitutes the interference filter so the corners of the square glass substrate do not behave as an  $H\alpha$  filter. Nevertheless this is probably the world's largest astronomical, narrow band filter. At the UKST plate scale this covers an on-sky area roughly  $5.7^\circ$  in diameter (slightly less than the full Schmidt field). To ensure complete and contiguous survey coverage with the circular aperture interference filter it was necessary to move use  $4^\circ$  field centres.

The filter central wavelength was set slightly longward of rest-frame  $H\alpha$  for two reasons, one instrumental and one astronomical. First, the UKST has a fast,  $f/2.48$  converging beam. This leads to the interference filter 'scanning down' in transmitted wavelengths for off-axis beams compared to beams incident normal to the filter. Secondly we wished to survey positive velocity gas (in our own and nearby galaxies). Given a band pass (FWHM) of  $70\text{\AA}$ , we chose to centre the filter at  $6590\text{\AA}$  in collimated light compared to  $6563\text{\AA}$  for rest-frame  $H\alpha$ . The peak filter transmission is around 90 per cent. Measurements of the filter at the CSIRO National Measurement Laboratory in Sydney quantitatively confirmed the excellent conformity of the filter to our original specifications (see Parker & Bland-Hawthorn 1998). First light filter images were obtained in April 1997.

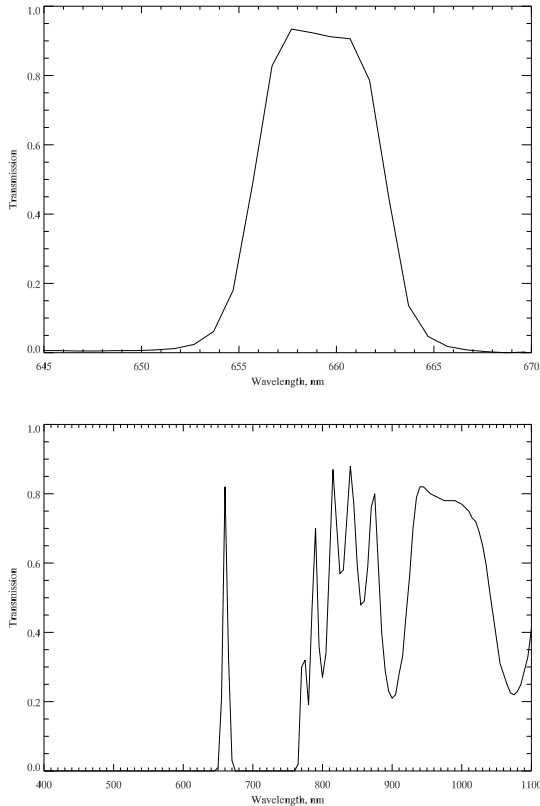


**Figure 3.** The upper plot (a) shows a high resolution transmission scan from central area of the H $\alpha$  filter. The lower plot (b) shows a wide wavelength range transmission scan from the central area of the H $\alpha$  filter showing the isolated narrow peak around H $\alpha$ . Transmission at longer wavelengths is not recorded in the survey data as the Tech-Pan film emulsion cut-off is at 6990Å and hence not sensitive to light at longer wavelengths.

#### 4.1 The filter model

Figure 3a-b shows two spectral scans of the filter, both taken near the centre using light at normal incidence. Figure 3a is the result of a high resolution scan around the H $\alpha$  region and shows that the bandpass is well centred on 6590Å and has  $\sim 70$  Å FWHM. The transmission is high across the reasonably flat top of the bandpass, reaching over 90 per cent. Figure 3b is based on a scan with an extended spectral range from 4000 to 11000Å. The CSIRO tests show that the out-of-band filter transmission is 0.01 per cent or less up to 7600Å. Figure 3b shows that the filter does transmit redward of 7600 Å at up to  $\sim 85$  per cent, but the survey data will be unaffected by this as the Tech-Pan film used as detector is insensitive beyond 6990 Å.

While this satisfies the intended performance of the fil-

ter in light of normal incidence, in the  $f/2.48$  beam of the UKST, light from an object in the field centre is focused into a cone and enters the filter at a range of angles up to  $11.4^\circ$ . The bandpass of an interference filter is blue-shifted for light entering at an angle. This was modelled by breaking down the contributions from the light cone into a series of concentric rings of size  $1^\circ$  covering the telescope beam over a range  $0.4^\circ$  to  $11.4^\circ$ , each entering the filter at a different angle. The contribution from the central part of the cone will not be significantly blue-shifted. The spectral shift was calculated for each ring according to Equation 1 adapted from Elliott & Meaburn (1976).

$$\lambda_\theta = \lambda_0 \cos(\arcsin(\sin(\theta)/\mu)) \quad (1)$$

Here  $\lambda_0$  is the chosen central wavelength for the filter bandpass in this case 6590 Å,  $\lambda_\theta$  is the shifted central wavelength of the filter profile based on the angle,  $\theta$ , of the incident light and  $\mu$  is the refractive index. A higher refractive index will minimise the blue shifting of the filter transmission with incident angle of light and the filter was designed with this in mind. Tests performed by the CSIRO using light at  $0^\circ$ ,  $5^\circ$  and  $10^\circ$  incidence found the effective refractive index of all the layers combined, ie. the effective monolayer, is  $\mu = 1.34$ . This is the value used in Equation 1 to generate the shifts for the spectral response of the H $\alpha$  filter in the UKST beam. These shifts are shown in Figure 4a. The solid lines are the shifting response curves with the most red response curve being applicable to light of normal incidence and the most blue response curve tracing the filter response to light entering at the most extreme angle from the telescope beam.

In order to combine these to generate a smeared filter response curve which accounts for the telescope beam, each shifted bandpass is weighted by the area of the contributing ring as a fraction of the whole cone. The weighted response curves are shown in Figure 4b and the resulting, summed bandpass is shown in Figure 4c. The FWHM of this smeared bandpass is 80 Å, centred on  $\sim 6550$  Å.

This models the transmission of the filter in the centre of a survey field. Towards the edges of the field the shape

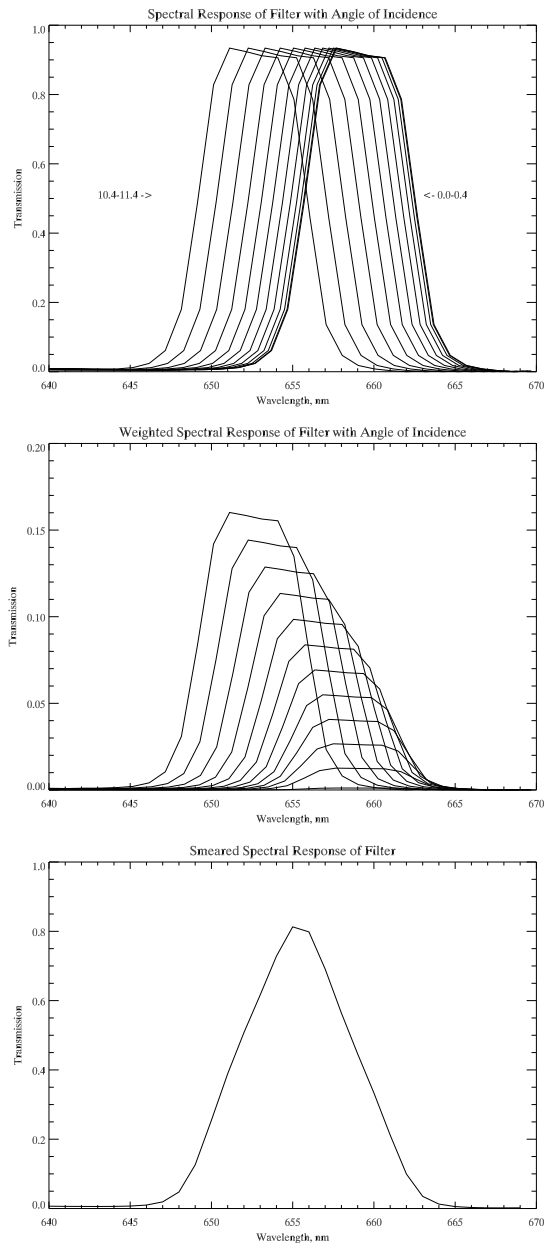


**Figure 4.** Blue-shifting response of interference filter in converging UKST beam as one moves out from the centre of the field. Top plot (a) shows the shift for each concentric ring of the beam, the second plot (b) shows these shifted response curves weighted according to the area of the ring. The final plot (c) shows the summed, smeared out filter transmission curve. The central wavelength of this smeared profile is 6550 Å and the FWHM is 80 Å.

of the cone changes and the maximum angle of incidence is over  $14^\circ$  which will shift the filter response further to the blue. The smeared out filter profile is significant as it permits calculation of the contribution of the contaminant [NII] lines at 6548 Å and 6584 Å, to the flux recorded by the survey. Based on the smeared out filter response shown in Figure 4c the filter transmits  $\text{H}\alpha\lambda 6563$  Å at 80 per cent,

[NII] $\lambda 6548$  Å at 82% and [NII] $\lambda 6584$  Å at 50 per cent. Given that the [NII] $\lambda 6584$  Å line is quantum mechanically fixed to be three times as strong as the [NII] $\lambda 6548$  Å line (Osterbrock 1989), this gives a transmission of 58 per cent for any [NII] emission compared with 80 per cent transmission for the  $\text{H}\alpha$  line. This is especially important when considering planetary nebulae (PNe) because the strength of the [NII] lines varies with respect to the  $\text{H}\alpha$  line from PNe to PNe and will have a very significant impact on any calibration scheme based on PNe line flux standards if not taken into account. Of course, for general diffuse  $\text{H}\alpha$  emission, the point to point  $\text{H}\alpha$  to [NII] ratio is in general unknown without independent spectroscopic information, so we assume a [NII]/ $\text{H}\alpha$  of 0.3, typically used for the warm ionised medium (e.g. Bland-Hawthorn et al. 1998).

## 4.2 Survey depth and quality control

The  $\text{H}\alpha$  films are not sky-limited after a 3-hour exposure, but this was chosen as a pragmatic limit which optimises depth, image quality and survey productivity. Field rotation and atmospheric differential refraction can adversely affect longer exposures (Watson 1984) which are also more susceptible to short-term weather and seeing variations. The associated 15-minute broad-band SR exposures were taken through the OG590 red filter. At this exposure level they are well matched to the depth of continuum point-sources on the matching  $\text{H}\alpha$  exposure. For completeness we include in Figure 5 the effective SR bandpass as a function of wavelength obtained from a calibration spectrogram for the OG590 filter in combination with the Tech-Pan emulsion.

With photographic surveys, the magnitude limit for a given survey field is not a fixed parameter but is a function of factors such as seeing, hypersensitisation and development of the films after exposure, emulsion batch variations and the brightness of the night-sky. Nevertheless, it is clear from comparison with the generally deeper, standard UKST R-band survey data, that the approximate magnitude limit for a typical  $\text{H}\alpha$  survey field in an equivalent R magnitude for



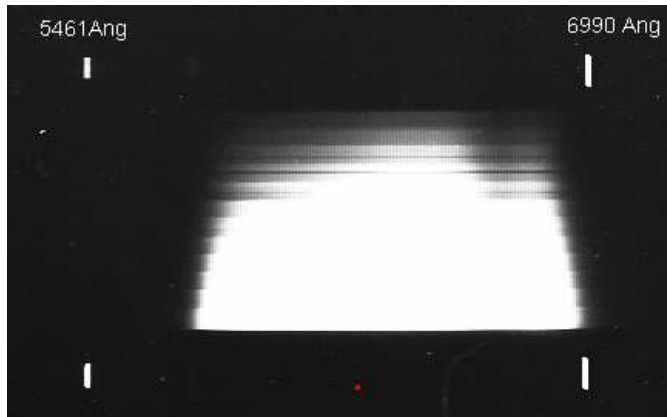


**Figure 5.** Calibration spectrograph result of the effective SR bandpass as a function of wavelength from the combination of the red OG590 filter and the Tech-Pan emulsion.

continuum point sources is  $\sim 20.5$  (Arrowsmith & Parker 2001). This value can be directly determined by examining the number magnitude counts from the matched H $\alpha$  SR and R band SuperCOSMOS Image Analysis Mode (IAM) data (see later) for a given field and determining the point where completeness breaks down. As an illustration we give magnitude limit estimates for continuum point sources in A and B grade exposures of two H $\alpha$  survey fields in Table 4.2.

Additionally, the use of the same emulsion for both H $\alpha$  and SR exposures ensures an excellent correspondence of their image psf's when film pairs are taken under the same observing conditions. The intention was to take the H $\alpha$  and SR exposures consecutively as far possible. This greatly simplifies the inter-comparability of both types of exposure. Of the 233 survey fields, only 100 are in fact sequential pairs while most of the rest were taken a few days apart. However 45 fields had a gap of one or more years between the H $\alpha$  and SR survey exposures because one or other of the exposures had to be repeated to satisfy the stringent survey quality acceptance criteria. Strict quality control has been applied to the survey pairs by M.Hartley and S.Tritton according to well established criteria before any exposure is allowed to be incorporated into the survey. This ensures that the most uniform and homogeneous data set possible is created. Each exposure grade is determined by means of a score with '0' being the best and '3' being the limit for an exposure to be considered an 'A' grade (highest quality). The image grade

**Table 2.** The depth of each of the four original images measured in R equivalent magnitudes.

Exposure Number	Survey field	Survey Grade	Histogram num/mag peak (R equiv. magnitude)
HA18745	h527	A2	$20.77 \pm 0.025$
HA17850	h527	BI3	$20.42 \pm 0.025$
HA18749	h678	A1	$20.62 \pm 0.025$
HA17935	h678	BIE4	$20.42 \pm 0.025$

is recorded in the information and data sheets which accompany the survey data, together with a letter code to indicate which is the most significant contribution to the score. Long, 3-hour exposures are prone to field rotation which can cause image trailing (denoted by T in the image grade), poor weather can lead to curtailed exposure times (U for underexposed). Cosmetic defects such as emulsion faults (E), haze halos (H) and processing streaks (P) can also contribute to a poor grade. These defects can be present in either the H $\alpha$  or the SR image. Where possible, any survey exposure which was not rated A grade was repeated. Unfortunately, a few B-grades had to be accepted into the survey though over 90 per cent were deemed survey quality, maintaining the high standards set for all UKST surveys.

## 5 ASTROMETRIC ACCURACY OF THE SHS

Astrometric calibration of survey photographic material measured on SuperCOSMOS is discussed in Hambly et al. (2001). The calibration procedure consists of applying a

six coefficient (linear) plate model to measured positions of Tycho-2 catalogue reference stars, along with a radial distortion coefficient appropriate to Schmidt optics (i.e.  $\tan r/r$ ) and a fixed, higher order two-dimensional correction map to account for distortion induced by mechanical deformation of the photographic material when clamped in the telescope plate holder to fit the spherical focal surface. As demonstrated in Hambly et al. (2001c), this yields absolute positional accuracy of typically  $\pm 0.2$  arcseconds for glass plates. The SHS, on the other hand, employs film media which cannot be as mechanically stable as glass on the largest scales. However, provided a sufficiently dense grid of reference stars is available, it is possible to map out the unique distortion pattern that any one film may present.

In order to achieve the best possible astrometry for the SHS, the generic SuperCOSMOS Sky Survey (SSS) astrometric reduction procedure was modified by replacing the averaged distortion map with a correction stage where the individual film distortion pattern is measured with respect to the UCAC astrometric reference catalogue (Zacharias et al. 2004). In Figure 6 we show the results of comparing first-pass SHS astrometry (i.e. without correction of any higher order systematic distortion) with the UCAC catalogue for a single SHS film. Residuals have been averaged in 1 cm boxes and smoothed and filtered using a scale length of 3 box widths. A systematic distortion pattern is clearly seen, and comparing with figure 1 of Hambly et al. (2001) there is no four-fold symmetry in the pattern, which is a characteristic of mechanical deformation of rigid glass plates. Moreover, similar plots for different films show different patterns, so a fixed correction map cannot be applied across the entire survey film set. Figure 7(a,b) shows histograms of the residuals of individual UCAC standards from which Figure 6 is derived; a robustly estimated RMS (i.e. a median of absolute deviations scaled by 1.48, to be equivalent to a Gaussian sigma) is found to be about 0.4 arcseconds. Now, if the SHS positional data are corrected during the astrometric reduction procedure using the map values displayed in Figure 6, the RMS drops to  $\sim 0.3$  arcseconds; the new histograms of

individual residuals are displayed in Figure 7(c,d). The value of  $\pm 0.3$  arcseconds can be taken as indicative of the typical global astrometric accuracy of the SHS in either co-ordinate, and compares favourably with the figure quoted for the SuperCOSMOS Sky Surveys (SSS) of  $\sim 0.2$  arcseconds, given the higher level of crowding of the SHS fields.

## 6 THE SURVEY SUPERCOSMOS DIGITAL DATA

The high speed ‘SuperCOSMOS’ measuring machine at the Royal Observatory Edinburgh (e.g. Miller et al. 1992, Hambly et al. 1998) has been used to scan the  $H\alpha$  and SR exposure A-grade pairs at  $10\mu\text{m}$  (0.67 arcsec) resolution. The same general scanning and post-processing reduction process is employed as for the directly analogous SuperCOSMOS broad-band surveys of the Southern Sky (SSS) currently on-line and outlined in detail by Hambly et al. (2001 a,b,c). The user interface is broadly equivalent and the main features are summarised neatly in Figure 1 of Hambly et al. (2001a). However, due to the special nature of the survey, some additional processing steps and  $H\alpha$  specific options have been added to create the on-line SuperCOSMOS  $H\alpha$  Survey (SHS) described below.

### 6.1 Basic characteristics of the on-line ‘SHS’ $H\alpha$ Survey

The Wide-Field Astronomy Unit (WFAU) of the Institute for Astronomy Edinburgh is responsible for maintaining the  $H\alpha$  survey data products. Both the  $H\alpha$  and SR data for the 233 Southern Galactic Plane survey fields are available on-line<sup>3</sup>. Unfortunately, there are no plans for the 40-field Magellanic Cloud  $H\alpha$  and SR survey pairs to also be put online. The data products are given as FITS files (see <http://heasarc.gsfc.nasa.gov/docs/heasarc/fits.html>) with comprehensive FITS header information detailing key photographic, photometric, astrometric and scanning param-

<sup>3</sup> <http://www-wfau.roe.ac.uk/sss/halpha>

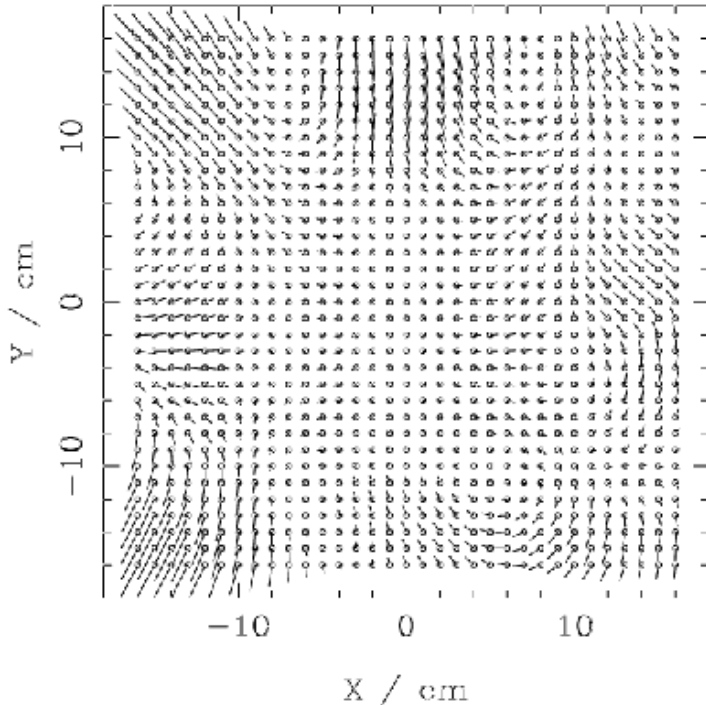


**Figure 6.** Systematic astrometric distortion pattern of SHS H $\alpha$  survey field h67, reduced using a standard six coefficient linear fit plus a radial distortion term, when compared to the UCAC catalogue. The scale size of the vectors is 0.5 arcsec to 1 cm. Systematic positional errors of more than 1 arcsec (corresponding to one tick mark on either axis) are observed in the film data, e.g. in the left-hand corners.

ters (e.g. Hambly et al. 2001b). The FITS images also have an accurate built-in World Co-ordinate System (WCS). This permits easy incorporation into other software packages such as the STARLINK *GAIA* environment for subsequent visualisation, investigation, manipulation and comparison with other data. The entire survey data are stored on RAID disks for fast access and a comprehensive set of web-based documentation has been provided. The pixel data map for each field is about 2 Gb. The scanned pixel data are processed through the standard SuperCOSMOS thresholded object detection and parameterisation software (e.g. Beard, MacGillivray & Thanisch 1990) to produce the associated Image Analysis Mode (IAM) data for each field. This process determines a set of 32 image-moment parameters which provide the astrometry, photometry and morphology of the detected objects. Full details of the image detection and parameterisation are given in Hambly et al. (2001b). For the SHS survey, a selection of the 32 most important IAM parameters from the merging of the H $\alpha$ , SR and I band data

for each detected image in the SHS are available and are given in Table 3.

The full resolution, 10 $\mu$ m pixel data and associated IAM parameterised data for both the H $\alpha$  and SR scanned exposures are stored on-line on a field by field basis. On the SuperCOSMOS web-site the scanned survey data for each field has the prefix ‘HAL’ before the survey field number (so H $\alpha$  survey field h350 = HAL0350 for example, when referring to the on-line digital SuperCOSMOS data). The SR images have been transformed to exactly match the pixel grid of the master H $\alpha$  exposures which permits direct image blinking and comparison between the pixel data for each field. The general H $\alpha$  survey data products are accessed via a web interface that has the same look and feel as the existing broad-band SuperCOSMOS on-line ‘SSS’ surveys but with some additional functionality. The IAM data produced for each field can be downloaded separately if desired or assembled into seamless catalogues on-the-fly which can cover several adjacent fields using the ‘Get a Catalogue’ option. The combined IAM data is organised into a full listing of 53

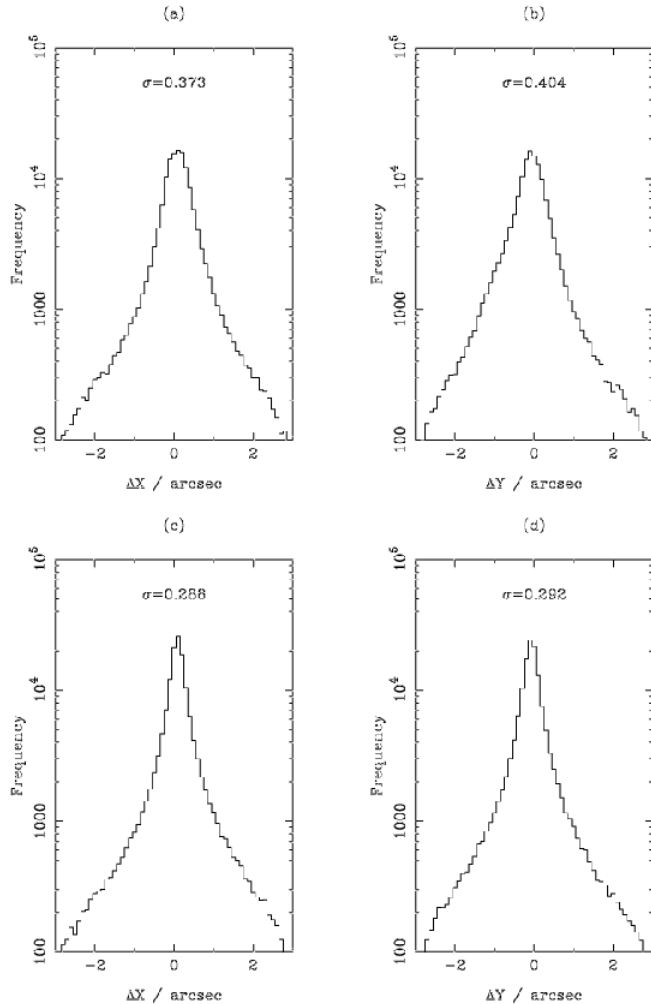


**Figure 7.** Histograms of residuals between SHS and UCAC astrometry (see text) for: (a,b) uncorrected positions, and (c,d) positions corrected during the astrometric reduction procedure using the distortion map shown in Figure 6. The accuracy is quantified by a robustly estimated RMS residual, in either co-ordinate, and shows a  $\sim 30\%$  improvement when the correction map is employed. From this analysis, SHS absolute astrometry is typically accurate to  $\sim 0.3$  arcsec.

image parameters or a more manageable subset of the most useful 32 as in Table 3. A set of ‘expert’ options are also available to further select catalogue extraction parameters. A special feature to create a difference image of each field following variable image psf matching techniques developed by Bond et al. (2001) also exists to permit large-scale resolved emission maps to be created with reduced artefacts from uncancelled stars. This can be computationally intensive and so is not generally available without prior arrangement with the Wide-Field Astronomy Unit. For most applications simple quotient imaging between the  $H\alpha$  and SR pixel data is sufficient due to the well matched psf’s and depth.

A  $16\times$  blocked-down version of each field is also avail-

able as both a GIF image and as a FITS file which has the WCS built in to the FITS header. These whole field maps can be studied to select smaller regions of interest for extraction at full resolution using the ‘Get an Image’ option. The full resolution pixel data access limit is currently set at  $9000 \text{ arcmin}^2$  with regions downloaded as FITS files (also with WCS) and both the SR and  $H\alpha$  data for the same region can be downloaded simultaneously. Areas for extraction can be chosen via equatorial (J2000 or B1950) or galactic ( $l, b$ ) co-ordinates in a variable  $m \times n$  arcminute rectangular region format. A clickable map of the current fields on-line enables individual field details to be displayed prior to viewing the blocked full field image. A batch mode enables large

**Table 3.** The selected 32 IAM parameters used in the merged SHS catalogue data

Number	Name	Type	Description	Units
1	RA	Double	Celestial Right Ascension	radians (FITS)
2	DEC	Double	Celestial Declination	radians (FITS)
3	EPOCH	Real	Epoch	year
4	l2	Real	Galactic longitude	dec.degrees
5	b2	Real	Galactic latitude	dec.degrees
6	R_Ha	Real	H $\alpha$ equivalent R-mag	mags
7	SR2	Real	matching SR magnitude (SR2)	mags
8	SR1	Real	First epoch SR magnitude (SR1)	mags
9	I	Real	First epoch I magnitude	mags
10	AREA_Ha	Integer	Total area H $\alpha$ image	pixels
11	AREA_SR2	Integer	Total area SR2 image	pixels
12	AREA_SR1	Integer	Total area SR1 image	pixels
13	AREA_I	Integer	Total area I image	pixels
14	ELL_Ha	Real	H-alpha image ellipticity	
15	ELL_SR2	Real	SR2 image ellipticity	
16	ELL_SR1	Real	SR1 image ellipticity	
17	ELL_I	Real	I image ellipticity	
18	PRFSTT_Ha	Real	H $\alpha$ N(0,1) profile classification statistic	0.001 sigma
19	PRFSTT_SR2	Real	SR2 N(0,1) profile classification statistic	0.001 sigma
20	PRFSTT_SR1	Real	SR1 N(0,1) profile classification statistic	0.001 sigma
21	PRFSTT_I	Real	I N(0,1) profile classification statistic	0.001 sigma
22	BLEND_Ha	Integer	H $\alpha$ Deblending flag (0 if not deblended)	
23	BLEND_SR2	Integer	SR2 Deblending flag (0 if not deblended)	
24	BLEND_SR1	Integer	SR1 Deblending flag (0 if not deblended)	
25	BLEND_I	Integer	I Deblending flag (0 if not deblended)	
26	QUAL_Ha	Integer	H $\alpha$ image Quality flag	
27	QUAL_SR2	Integer	SR2 image Quality flag	
28	QUAL_SR1	Integer	SR1 image Quality flag	
29	QUAL_I	Integer	I image Quality flag	
30	PA	Integer	Celestial position angle (selected band)	degrees
31	CLASS	Integer	Classification flag (selected band)	
32	FIELD	Integer	SHS field number (4 $^\circ$ centres)	

numbers of thumb-nail images to be extracted around objects of interest with the option to return H $\alpha$  and/or SR postscript plots of the extracted images. An option to apply a ‘Flat-Field’ to the H $\alpha$  pixel data in intensity space is included to permit correction of the non-uniformities in the measured exposures arising from the excellent but slightly varying H $\alpha$  filter transmission profile. This has been shown to work effectively and is described in Section 9. A radius of 153 mm ( $\sim 2.85$  degrees) from each survey field centre has been adopted as the region with good data ( $< 15$  per cent correction factors). The ‘good data’ radius from each scanned H $\alpha$  field centre has been used in creating a confidence map which is incorporated into the extracted FITS image as an additional FITS extension (extension [3], e.g test-image.fits[3]). This can be used to flag areas of the extracted image that might not be quite as good as others.

Currently this has values of 100 for regions extracted interior to this radius and 0 for regions outside.

### 6.2 Incorporation of the SSS ‘I’ band data

The IAM catalogue downloaded directly via the ‘Get a Catalogue’ option or as incorporated in the FITS table extension to the downloaded pixel data via the ‘Get an Image’ option, contains information not just from the H $\alpha$  and the SR images but also from the SERC-I (near infrared) survey which has been carefully matched in with the SHS data. The I-band data is particularly useful when searching for point-source H $\alpha$  emitters as it can help to eliminate contamination from late-type stars. However there are issues that any user should be aware of when combining the I-band data with the SHS magnitudes. When calibrating UKST data, positional and magnitude-dependent systematic errors are present as a result of variations in emulsion sensitivity and vignetting to-

wards the image corners (Hambly et al. 2001b). The I-band survey was taken on standard ESO/SERC  $5^\circ$  field centres, so the vignetting will have a different effect on the two sets of photometry at a given survey location. Furthermore, the I-band data are calibrated to relatively few standards. These differences are evident when looking at a plot of SR magnitude versus  $R - I$  colour derived from the SR and paired I-band photometry. Figure 8 shows two colour magnitude diagrams (CMD) for stars taken from a 10 arcminute region centred on the middle of SHS field h1109 in Monoceros where the low galactic reddening of  $E(B - V) = 0.24$  (Schlegel, Finkbeiner & Davis 1998) should leave the  $R - I$  colour roughly constant for much of the observed magnitude range. Figure 8a shows the raw result, where a large, unphysical variation of 3.5 magnitudes is seen in the  $R - I$  colour from the brightest to the faintest objects. This is removed as a first-order correction from the survey data by selecting a master colour, in this case the SR, and correcting the I-band across all survey fields. Note however that at fainter limits one in fact expects redder  $R - I$  colours as such stars are likely to be further away and prone to be more dust reddened or intrinsically fainter and therefore more likely to be late types. Hence some modest slope is expected. Figure 8b shows the CMD for the same patch of sky after the colour correction has been applied, giving a result in better agreement with expectation. The data can be downloaded in corrected or uncorrected form via an option in the ‘‘Expert’’ parameters of the SHS website. It is important to ensure that the I-band correction is not applied inappropriately, i.e. in a field of intrinsically high reddening, as such a correction will remove genuine features from the data. It should be used with caution.

## 7 SHS POINT SOURCE PHOTOMETRY

A significant advantage of the SHS data over its rivals is the ability to detect point sources which have been photometrically calibrated to CCD standards (e.g. Boyle et al. 1995, Croom et al 1999). With measurements of isophotal mag-

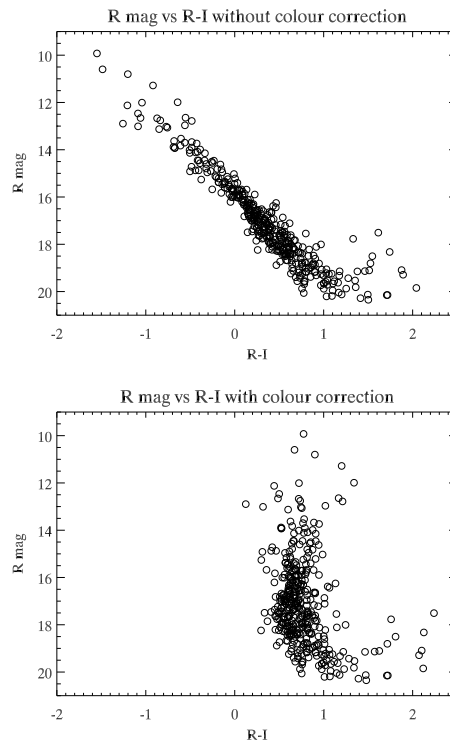


**Figure 8.** Plots of SR magnitude versus  $R - I$ , from a 10 arcminute square region in Monoceros, before colour correction for positional and magnitude dependent errors (a - upper) and after (b - lower).

nitude and object classifications, it is possible to apply a photometric calibration to the  $H\alpha$  and SR films by comparing the SuperCOSMOS raw magnitudes of stars from the Tycho-2 Catalogue (Hog et al. 2000) and the Guide Star Photometric Catalogue (Lasker et al. 1988). These in turn are checked against photometric standards derived from the CCD observations given by Croom et al. (1999) and Boyle et al. (1995). The narrow-band  $H\alpha$  images are calibrated to an ‘R-equivalent’ scale. The 3 hour  $H\alpha$  and 15 minute SR exposures are matched so that both reach similar depths of  $m_R \simeq 20.5$  for point sources. Where an object is detected in one band but not in the other a default value of 99.999 is given in the catalogue data for the magnitude in the missing bandpass. Positional and magnitude dependent errors are seen in the raw photometric data, created by varying transmission profile and diffraction effects through the thick (5.5 mm)  $H\alpha$  filter, but these are corrected for in the data available through the SHS website by comparison with the SR data. Photometric consistency is achieved by using the

overlap regions between fields to match zero-points across the survey. These corrected magnitudes provide a means of selecting point-source emitters. The variations in measured IAM stellar parameters as a function of field position arising from the variable psf from field rotation, vignetting etc, especially at large radii from the field centres, requires that such selection is performed over limited 1-degree areas. In this way stars with an emission line at H $\alpha$  will show an enhanced H $\alpha$  magnitude compared with the SR magnitude. At the bright end of the magnitude distribution, severe photographic and SuperCOSMOS saturation effects come in to play, limiting stellar photometry to R of about 11-12 in both the H $\alpha$  and SR pass-bands.

## 8 SPURIOUS IMAGES IN THE SHS

Spurious images appear from time to time in all photographic images scanned by SuperCOSMOS. They have a variety of forms and causes and are present in images extracted from the SSS as well as SHS. They can sometimes be picked up by examination of the pixel images directly, though they are often missed, and can also appear as spurious detections in the IAM data. They have a variety of sizes and shapes and may be in or out of focus depending on whether the contaminating source is on the emulsion surface or on the platten used by SuperCOSMOS to sandwich the film flat for scanning. Here, we differentiate between spurious images in the emulsion itself caused by processing defects, emulsion flaws and static marks, and those caused by foreign objects on the surface of the emulsion or on the back of the film. Holes and scratches in the emulsion surface can also give rise to spurious images. Satellite trails and transient phenomenon also give rise to real developed images which may have no counterpart in other survey bands of the same region. We do not consider these here.

### 8.1 Basic causes

The SuperCOSMOS facility is situated in a class-100 clean room and each film is pressure air-cleaned prior to scan-

ning. However, despite best efforts, particles that may already have been present on the emulsion before shipment to SuperCOSMOS manifest themselves as spurious images. The biggest cause is fine particulate dust (20–100 $\mu$ m). Unfortunately the Estar film base of the Tech-Pan emulsion is prone to static charge build-up.

### 8.2 Recognising spurious images

The SuperCOSMOS scanning system is highly specular so detritus present on the emulsion surface that is often invisible when viewed under diffuse illumination conditions (such as on a light table) is revealed in sharp relief in the SuperCOSMOS data. The number of artefacts seen in the SHS data is somewhat worse than on other glass plate based surveys of the SSS. Fortunately, having matched exposures in two bands makes identification of such artefacts more straightforward. For example, since the H $\alpha$  and SR exposures are registered on the same pixel grid, quotient imaging can reveal the locations of spurious images. A 5 $\times$ 5 arcminute region extracted from h273, a field with a particularly high number of spurious images, is shown in Figure 9.

We can take advantage of the fact that the pixel image properties of spurious images are usually quite distinct from real astronomical images, often having a sharpness below that possible from the combination of telescope optics and seeing disk. Their shapes are often highly irregular and non-symmetrical such that they would not fit any normal psf. This makes them amenable to Fourier filtering. Objects that have no counterpart in the other band are potential spurious image candidates though variable objects, novae and the effects of de-blending complicate the issue significantly. Various IAM parameters such as the profile statistic, ellipticity etc. may also aid in identification. Furthermore, spurious IAM objects arising from de-blending overlaying contaminating fibres or hairs usually have very high ellipticities which may help in isolating likely candidates. Storkey et al. (2004) discuss techniques for recognising and eliminat-

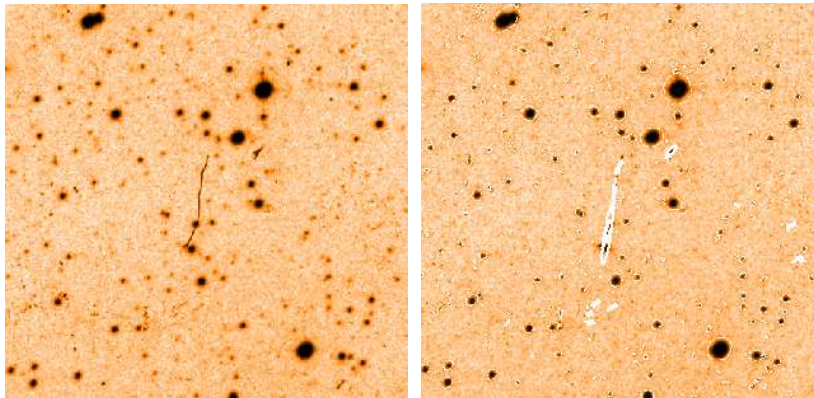


**Figure 9.**  $5 \times 5$  arcminute extracts of SuperCOSMOS  $H\alpha$  data from SHS survey field h273 highlighting a contaminating spurious image together with a matching image with the IAM data overlaid and with all the spurious images in the frame highlighted.

ing spurious objects in the on-line SuperCOSMOS surveys. As yet this procedure has not been applied to the SHS data.

## 9 FLAT-FIELDING OF THE SURVEY DATA

For any interference filter of the size used here, low-level non-uniformities exist which lead to residual non-physical background variations in the exposed images. In order to establish the magnitude of such effects, three flat-field exposures were taken with the filter subject to uniform illumination. The flat-field images permitted evaluation of the combined effects of filter transmission in the fast,  $f/2.48$  Schmidt beam and telescope vignetting (see UKST Unit handbook, Tritton, 1983). The flat-field images were exposed to place them on the linear portion of the film's characteristic curve and were averaged to give the filter/telescope transmission profile shown in Figure 10a-b.

Figure 10a shows transmission contours at 85, 90, 92, 95, 97 and 98 per cent of maximum transmission in the central region. The response is seen to be asymmetric, with the 97 per cent contour extending beyond the edge of the  $5.16^\circ$  field on the right, which corresponds to the west of the survey fields. In the east the transmission decreases more rapidly, reaching 85 per cent at the eastern edge. Towards the filter corners the transmission drops further. However, the  $4^\circ$  overlapping centres (Section 4) and the asymmetric nature of the response allows the selection of  $H\alpha$  data requiring flat-field correction of less than 15 per cent for any

given area of sky, provided that adjacent fields are available. Most data will require much smaller flat-field corrections. The effect of flat-field corrections as large as 15 per cent on pixel data is considered in the survey calibration section. Figure 10b is a histogram equalization of the actual flat-field pixel map which reveals the extremely low level artefacts present at the 0.1 per cent level which are invisible in a linear rendition. The flat-field correction has been stored as a transmission array with maximum value unity, so it is applied by dividing survey image values in intensity space by the relevant correction array elements. This is available as the default option on the SHS website. The correction breaks down towards the corners of the scanned image and in regions outside of the clear aperture because the density of the exposures at the edges of the circular aperture is too low to lie on the straight line portion of the characteristic curve leading to an over-correction and also because the  $H\alpha$  filter transmission is becoming increasingly skewed in these extreme regions. Raw transmission or photographic density values and generically calibrated intensity values without flat-field correction can also be requested on the download form. The IAM data is obtained from the raw SuperCOSMOS scans without flat-field correction.

### 9.1 Specific filter features

Despite the superb quality of the filter, low-level, large-scale variations in transmitted flux can be seen in the  $H\alpha$  sur-



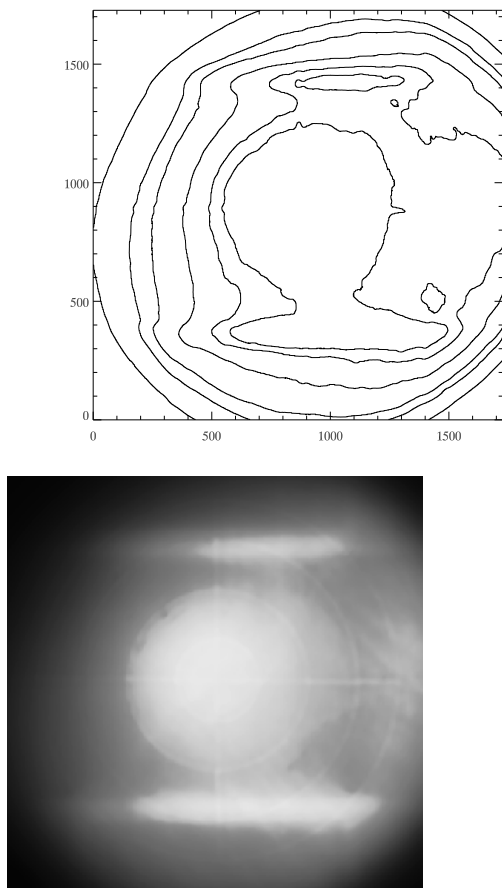


**Figure 10.** (a - top) Contour plot of the narrowband H $\alpha$  filter transmission over the SuperCOSMOS scanned area of  $5.156^\circ$  ( $1728 \times 1728$  pixel). The contours are plotted at 85, 90, 92, 95, 97 and 98 per cent. The bottom image (b) is a histogram equalisation of the same flat-field data which reveals the filter artefacts present at the 0.1 per cent level

vey images under certain exposure conditions. In particular there are two parallel bands of slightly enhanced transmission (leading to elevated photographic density) going E-W in the north and south of the filter. These bands are only 1–3 per cent higher in intensity than the surrounding regions. A series of low-level artefacts which are not obvious in the contour plot because they are at a level of  $< 1$  per cent can just be discerned in the filter transmission image in Figure 10a-b. They can also just be seen in the contour plot as the spike in the 98 per cent contour just right of centre. The observed shape of these artefacts mimics the series of shallow concentric grooves scored into the surface of the mandrel to enable the Tech-Pan film to be sucked under light vacuum to the curved focal surface of the plate-holder

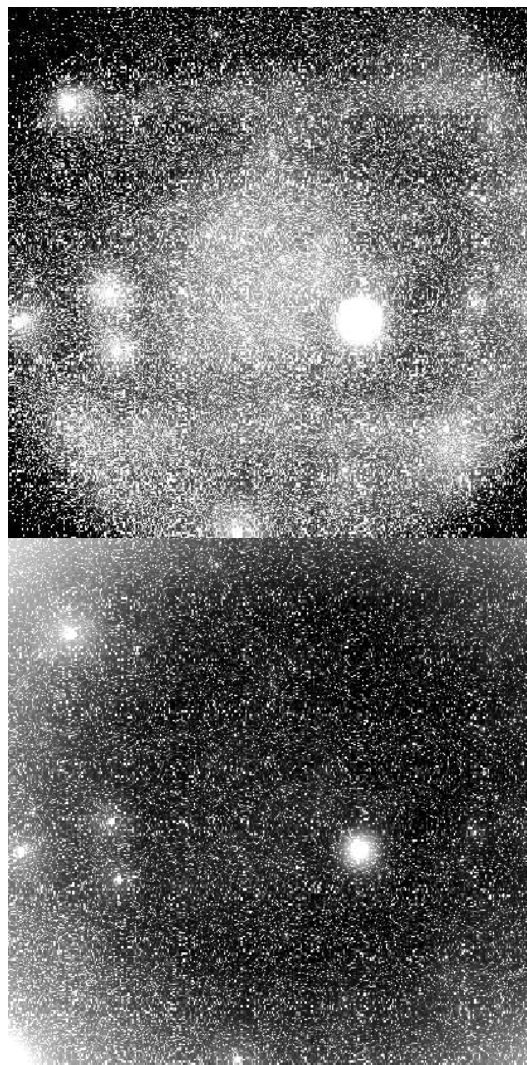


**Figure 11.** Two  $16 \times$  blocked down,  $5.156^\circ$  SHS H $\alpha$  images of field h410. The top image (a) is the raw intensity data without flat field correction. The bright areas trace not Galactic emission but the filter transmission profile seen in Figure 10. The bottom image (b) has had the flat-field correction applied which successfully removes the filter artefacts from within the circular aperture.

to ensure proper focus. They are thought to arise from the backscattering off these grooves of light that has passed right through the film. Again, it is gratifying that these artefacts, present at the  $< 0.1$  per cent level, are effectively removed by application of the flat-field.

## 9.2 Application of the flat-field and correction validity

Field h410, which sits away from the Galactic Plane on the extreme edge of the survey at  $(l, b)$   $330.2^\circ, +10.28^\circ$  has been chosen to test the validity of the flat-field correction as

it contains a very low-level isotropic background of Galactic line emission. In the survey image this will be moderated by the filter response. Figure 11a-b shows two  $16\times$  blocked down images of survey field h410. The top image Figure 11a is the raw  $H\alpha$  data, before the application of the flat-field correction. The structure evident on the field as lighter areas is not Galactic emission but matches the filter transmission profile. The two horizontal bars are present and the image is less exposed towards the corners where the recorded intensity is lower and the star density also falls. The bright star just to the right of centre is  $\epsilon$  Lupi.

Application of the flat-field correction results in Figure 11b which should have a flat background wash of emission across it. The structure from the filter is no longer evident and the bright areas are now in the corners, where the larger flat-field correction over-corrects the SuperCOSMOS intensity counts. This will not adversely affect the majority of the pixel data available on the SHS website. Data can always be taken from the best area of filter response and no flat-field correction larger than 15 per cent is necessary for any of the survey data that overlap a neighbouring field. Data from the edge of the survey, where no adjacent field exists, have been made available and may require a correction greater than 15%. Areas affected in this way are flagged in the third extension table which accompanies the downloaded FITS image.

## 10 GEOCORONAL $H\alpha$ EMISSION

Geocoronal  $H\alpha$  emission is caused by fluorescence after solar Lyman  $\beta$  excitation of atomic hydrogen in the exosphere. Because imaging surveys lack velocity resolution for the emission they record, the geocoronal contribution will be present in all of them but indistinguishable from bona fide Galactic  $H\alpha$  emission. Fortunately, one modern  $H\alpha$  survey, WHAM (e.g. Haffner et al. 2003), offers very good velocity resolution ( $\sim 12$  km/s) and is able to separate the atmospheric emission from the Galactic emission and measure the intensity. Nossal et al. (2001) report on  $H\alpha$  observations car-

ried out by the WHAM instrument in 1997, the same time as the SHS imaging was starting at the UKST. They find that the geocoronal emission intensity depends on how much the earth shades the line of sight from sunlight. Their resulting plot of geocoronal  $H\alpha$  emission as a function of earth shadow height shows that at heights greater than 6000 km only a very low level  $\sim 2$  R wash of geocoronal  $H\alpha$  emission is present. Based on the observational information available in the headers of the SHS images, it is possible to calculate the shadow heights for any field. For a random sample of 6 SHS fields the shadow height for the whole three hour observation and across the five-degree field of view was found to be greater than 6000 km, so low-level geocoronal emission is not problematic, as most Galactic Plane fields covered by the SHS will contain significantly stronger emission.

## 11 APPLICATION OF AN ABSOLUTE CALIBRATION TO THE $H\alpha$ SURVEY DATA

The AAO/UKST  $H\alpha$  survey data needs an absolute intensity calibration if the full scientific value of its sensitivity to faint, diffuse emission is to be realized. The intensity calibration must provide a reliable means of transforming the pixel intensity values from SuperCOSMOS scans of the  $H\alpha$  images into meaningful intensity units such as Rayleighs which is consistent from field to field. We show that continuum emission can be successfully removed from the  $H\alpha$  images by scaling and subtracting the SR continuum image. Unlike CCD data, which enjoys a linear response over a wide range of emission strength, photographic data can be very difficult to calibrate because the response of the emulsion and SuperCOSMOS scanner is linear only over a relatively small dynamic range. Variations in sensitivity and background occur from exposure to exposure, especially when the  $H\alpha$  and SR pairs were taken on different nights, phases of the moon etc. Despite this, we show that the survey data have been well exposed to capture Galactic emission on the linear part of the characteristic curve and can be calibrated by means of comparison with the complementary, accurately intensity

calibrated SHASSA survey (Gaustad et al. 2001). This process does not form part of the current SHS release but can be undertaken by the user as required.

### 11.1 Image comparison with SHASSA

The Southern H $\alpha$  Sky Survey Atlas by Gaustad et al. (2001) provides wide-field narrow-band CCD H $\alpha$  images of the southern sky below  $\delta = +15^\circ$  taken with a robotic imaging camera sited at Cerro Tololo Inter-American Observatory (CTIO). The camera used a small, fast, f/1.6 Canon lens which gave a very large ( $13^\circ$ ) field of view and a spatial resolution of 48 arcseconds. Each SHASSA field was imaged through a narrow-band interference filter of width  $32 \text{ \AA}$  centred at  $6563 \text{ \AA}$  as well as a continuum filter with two bands of  $61 \text{ \AA}$  at  $6440 \text{ \AA}$  and  $6770 \text{ \AA}$ , on either side the H $\alpha$  line. The SHASSA website<sup>4</sup> makes available the raw H $\alpha$  and continuum images as well as 48 arcsecond and 4 arcminute resolution continuum subtracted, intensity calibrated data. The SHS data is superior in terms of resolution while the general sensitivity of both surveys appears qualitatively similar for large-scale emission features. For example, in Figure 12 we present SHS and SHASSA images of the HII region RCW 19.

### 11.2 The SHASSA intensity calibration

The SHASSA intensity calibration was derived from the planetary nebula spectrophotometric standards of Dopita & Hua (1997) after the continuum images had been scaled and subtracted from the H $\alpha$  frames. Aperture photometry for eighteen of the bright PNe standards was measured from the SHASSA images and used to calculate the calibration factor for the whole survey. A difficulty in applying PNe line fluxes to H $\alpha$  narrow-band imaging is the proximity of the two [NII]  $\lambda\lambda 6548, 6584$  lines which are included in the flanks of the SHASSA H $\alpha$  filter bandpass. These vary in strength relative to H $\alpha$  between PNe and could significantly affect the result. Calculating the transmission properties of

the interference filter to these lines is complicated by the blue-shifting of the bandpass with incident angle, an effect which must be treated carefully in the SHS data as the filter sits in the fast f/2.48 beam of the UKST. This problem is not as severe for the SHASSA data because in this case the filter sits in front of the camera lens, leaving only the effects of the very large field of view. These effects are considered in Section 4 of Gaustad et al. (2001) and carefully accounted for in their calibration.

To allow a more detailed comparison, aperture photometry for 87 PNe with a range of surface brightness and integrated flux and with an independent measure of H $\alpha$  flux, was carried out on SHASSA images. Published spectroscopic data were used to deconvolve the contribution from the [N II] lines passed by the SHASSA filter. The results agree with published data to  $\Delta F(\text{H}\alpha) = -0.01\text{dex}$ ,  $\sigma = 0.05$  for SHASSA minus literature fluxes (Frew 2005, in preparation; cf. Pierce et al. 2004). Since the PNe literature fluxes have associated errors, the SHASSA calibration is better than  $\pm 10$  per cent across the whole survey, in agreement with the nominal error supplied by Gaustad et al. (2001).

An additional uncertainty is introduced to the zero-point of the SHASSA intensity calibration from the contribution of geocoronal emission. Gaustad et al. (2001) estimate this by comparison with overlapping WHAM data points and interpolating where there are none. Our check of the intensity calibration against independent flux measures of planetary nebulae indicates that the geocoronal contribution to the SHASSA H $\alpha$  images has been successfully removed. Finkbeiner (2003) also showed there is no significant offset between WHAM and SHASSA data. So we conclude that the SHASSA data has been well calibrated to a zero-point consistent with independent measurements and therefore have confidence in its use as a baseline calibration for the SHS data.

<sup>4</sup> <http://amundsen.swarthmore.edu/SHASSA/>

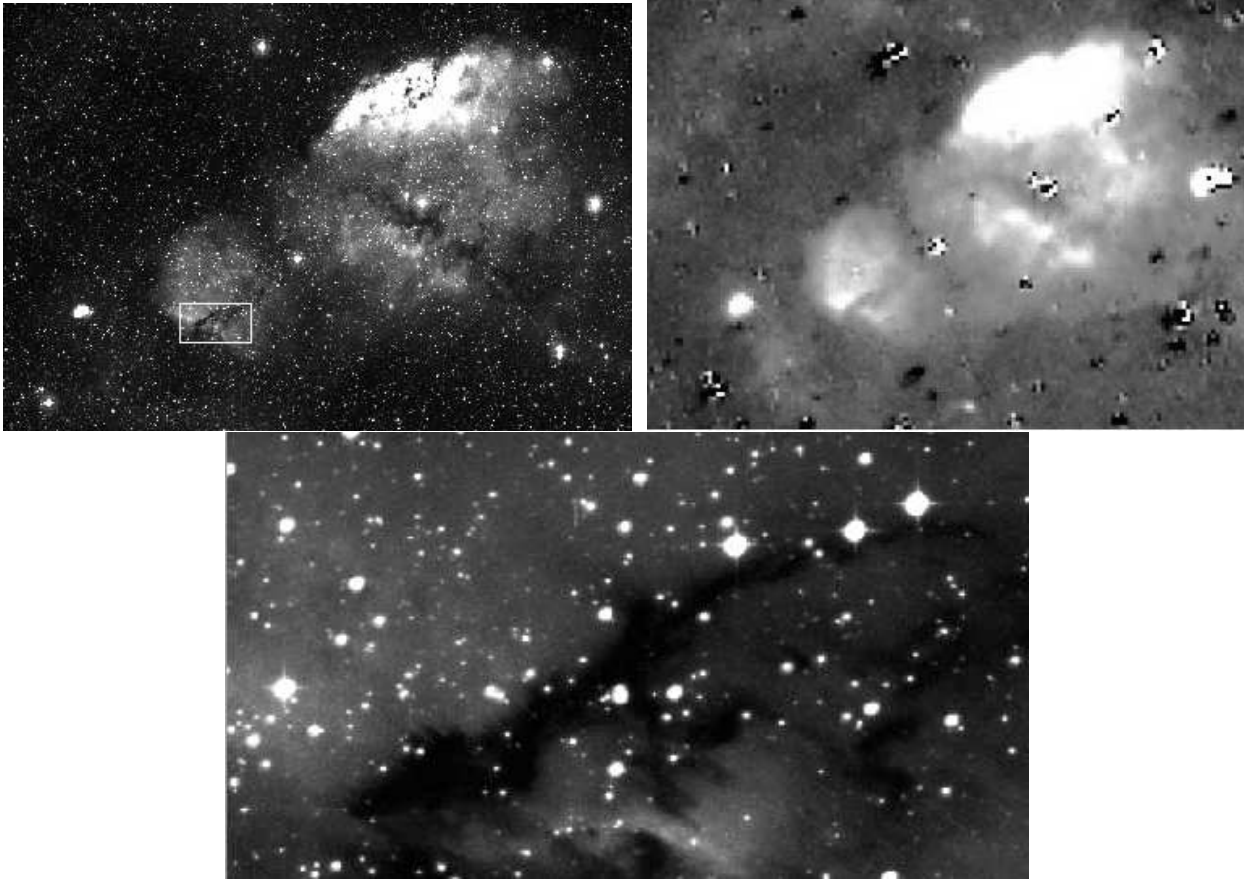


**Figure 12.** An  $105 \times 75$  arcminute region centred on well known HII region RCW 19 (GUM 10) at  $\alpha, \delta = 08^h 16^m 17^s, -35^\circ 57' 58''$  (J2000) extracted from the SHS survey (top left) and the equivalent SHASSA region (top right). A full resolution  $8.3 \times 4.6$  arcminute region from the SHS survey data is shown below centred on the southern HII region component at  $08^h 19^m, -36^\circ 14'$  and indicated in the lower resolution SHS image with a rectangle.

### 11.3 Continuum Subtraction of the SHS

Diffuse emission recorded through the narrow-band  $H\alpha$  filter on the Tech-Pan films will be a combination of Galactic  $H\alpha$  line emission, continuum emission, night-sky auroral lines and geocoronal emission. Ideally all of these components would need to be disentangled to extract just the Galactic  $H\alpha$  emission. In practice the geocoronal and auroral emission is considered as a low ( $\sim 2$  R) level but temporally varying uniform wash which simply elevates the general background on each exposure to a slightly varying degree.

The matching SR images provide a measure of the continuum component and, properly scaled, can be used to produce continuum subtracted  $H\alpha$  images. Although the  $H\alpha$  and SR exposures are generally exposed to attain the same depth for continuum point sources, the nature of photography and the vagaries of the observing conditions (e.g. if

the exposure pairs were not contemporaneous and taken in different moon phases or if the seeing changed) mean that the depth and image quality between the  $H\alpha$  and SR exposures can and does vary. Hence it is necessary to determine a continuum subtraction scaling factor between  $H\alpha$  and SR on a field by field basis. This factor must be precisely determined for the continuum subtraction to be effective. For high-dynamic range CCD exposures, the standard method for determining the appropriate scaling factor to subtract continuum from narrow-band is to compare aperture photometry for stars on both images whose exposures are normally interleaved on short timescales.

Unfortunately, this does not work well with the  $H\alpha$  SR film exposure pairs (Pierce 2005), often leading to under or over-subtraction of the continuum. This arises due to varying backgrounds on the film exposures caused by; low-level

emulsion sensitivity variations between films (especially if they come from different hypersensitised batches), inherent chemical fog variations in the emulsion, processing variations and true sky background variations arising for the reasons given above. These varying backgrounds result in the same magnitude stars saturating at different levels on different exposures as their Gaussian point spread functions are superimposed on top of any diffuse emission and elevated background which can severely truncate their peaks. The limited dynamic range of SuperCOSMOS also acts as a further low ceiling above the background, which leaves little room for these bright stellar Gaussians making it hard to effectively utilise stellar photometry to determine the correct scaling factors.

Fortunately, we are able to use the existing SHASSA data to provide a well-determined scale with an independently confirmed zero-point to compare with and calibrate the SHS images. Even exposure pairs taken years apart can be successfully continuum subtracted. A detailed investigation of the SHS calibration process has been undertaken by Pierce (2005) but the essential aspects of this process and its application are given here. For example, Figure 13 shows three images of a 30 arcminute region taken from field h350, which shows strong, varying Galactic H $\alpha$  emission. The top image is the H $\alpha$  image downloaded from the SHS website, the middle image is its SR counterpart while the bottom image has had the SR ‘continuum’ image scaled and subtracted via a comparison with SHASSA data. In general this subtraction is very good, removing most of the stellar images and the diffuse continuum. Only the stars which sit in the strongest emission have been over-subtracted and appear as white spots in the image.

For a given area of sky, pixel data from each survey can be downloaded and, after matching for spatial resolution, the SuperCOSMOS intensity counts can be compared directly with the Rayleigh values in the SHASSA data. A plot of continuum-subtracted SHASSA pixels against equivalent SHS pixels should return a linear relation with a common zero point if the reduction and intensity calibra-



**Figure 13.** 30 arcminute region at  $16^h 47^m, -49^{\circ}00'$  (J2000) from near the centre of SHS field h350 with bright areas of emission shown darkest. The top image is the raw H $\alpha$  image, the middle the matching SR while the bottom image is a continuum-subtracted image of the same area. The subtraction, based on a comparison with SHASSA data, has worked well, leaving only minor residuals around stars on the bright diffuse emission.

tion have been properly carried out. Comparing incorrectly continuum-subtracted SHS data with SHASSA data results in an offset between the two surveys. A range of values for the scaling factor can be applied to the SHS data until the zero-point of the continuum-subtracted UKST survey images best matches the zero-point of the equivalent SHASSA data, indicating the appropriate value to use. A calibration based on the SHASSA data will provide an advantage for the SHS over the CTIO survey as it can be applied to the full resolution pixel data. This offers the chance to determine intensities for emission structures not resolved by SHASSA such as the new sample of extended PNe discovered from the SHS data (e.g. Parker et al. 2003, 2005, Pierce et al. 2004, Frew & Parker, in preparation and see Section 14.1).

Each scanned SHS survey field, at the full 0.67 arcsecond resolution, contains over 2 Gb of data so it was not practical to download and compare all the pixel data for each field. Instead, most of the emission variation on a given survey field can be sampled using carefully selected 30 arcminute regions. For fifteen fields, several 30 arcminute areas were downloaded to sample the complete dynamic range of emission present. Once the scaling reliability over a range of flux levels and central aperture locations was established, the best single, 30 arcminute region was chosen from the whole frame for the rest of the 233 survey fields to provide the base calibration for each field. The H $\alpha$  filter flat-field correction was applied to remove the low-level non-uniformities in transmission across the narrow-band filter.

Data requiring a flat-field correction of up to 15 per cent have been shown to be suitable for inclusion in the survey, though in most cases data returned from the SHS website require less correction than this. For the regions considered here, the pixel data only required flat-field correction  $\leq 3$  per cent in most cases and, in general, no more than 8 per cent. For two fields, h350 and h1109 regions well away from the best area of the filter were also selected to confirm that the pixel data behaves as expected when larger flat-field corrections are required. The results are discussed below.

#### 11.4 The SHS Calibration process

A detailed description of the SHS survey calibration process based on zero-pointing each SHS field to SHASSA is given in the thesis of Pierce (2005). The essentials of this scheme are described here. Each SHS field is completely covered by just one 13° SHASSA field and data from the best area of SHASSA filter response was chosen for comparison with the SHS images. For direct comparison, the H $\alpha$  and SR SHS data at 0.67 arcsecond was re-binned to match the 48 arcsecond SHASSA pixels using the IDL routine HREBIN<sup>5</sup>. This returns the mean value of the 72  $\times$  72 full resolution SHS pixels that constitute a single SHASSA 48 arcsecond pixel, so the calibration factor determined from the comparison plot applies to the full resolution SHS data. At this coarse resolution the SR data was scaled and subtracted from the H $\alpha$  image. Because the correct scaling factor was not yet known, a range of scaling factors from 0.4 to 2.0 was applied so that the best value could be selected by matching the SHASSA zero-point. The equivalent area of SHASSA data was selected, aligned and trimmed to match using the IDL, HASTROM routine. These images were then compared directly, pixel by pixel, with the re-binned, continuum-subtracted SHS data to give a plot of SHASSA values in Rayleighs versus SuperCOSMOS counts per re-binned pixel. The linear portion of the resulting comparison was then fitted to determine the number of SuperCOSMOS counts per 0.67 arcsecond pixel per Rayleigh. Averaging SuperCOSMOS data in this way only works properly if all the SuperCOSMOS pixels are on the linear portion of the characteristic curve at the faint end and unsaturated at the bright end. Once the SuperCOSMOS dynamic range is exceeded pixel saturation arises and the SHASSA to SuperCOSMOS linear relation breaks down as the SuperCOSMOS flux becomes increasingly underestimated (e.g. Phillipps & Parker, 1993) as seen in Figure 17.

The adopted process was followed for the same 30 ar-

<sup>5</sup> Interactive Data Language: <http://www.rsinc.com>

cminute region from SHS field h350 as shown in Figure 13. The upper image in Figure 14 shows the SHS image with the continuum-subtracted at 48 arcsecond resolution. The lower image is the trimmed and aligned SHASSA data. Bright stars on the continuum subtracted SHASSA images leave significant residuals while in the SHS data any stellar residuals are barely visible and then only for the very brightest stars. The pixel-to-pixel comparison plot for this area is shown in Figure 15. Each point on this plot is the pixel value from the SuperCOSMOS scan against the Rayleigh value from the SHASSA data. Immediately, it can be seen that the SHS data follows a tight linear relation with the SHASSA values over a range of several hundred Rayleighs. The outliers from this distribution at around 4000 SuperCOSMOS counts correspond to the SHASSA stellar residuals noted from Figure 14.

A further nine 30 arcminute areas were examined from field h350 to cover the whole dynamic range of diffuse emission evident in the field. Figure 16 shows the 16 $\times$  blocked down H $\alpha$  image for this field with contours of filter response overlaid and boxes indicating the areas used. The large area of strong emission in the west of this field is caused by the UV flux from OB association Ara 1A A (Mel’Nik & Efremov 1995). In all but two cases the areas were selected from the best area of the filter response, the exception being the two areas extracted from the SE corner which were included to test the effect of using pixel data from the edge of the SHS survey fields where the flat-field correction is larger.

Figure 17 shows the resulting SHASSA versus SHS comparison plot with differently shaded points belonging to different 30 arcminute areas. Almost the full range of the SHS data is shown, with the pixel values showing a good linear relation to the SHASSA data from the faintest emission on the field at  $\sim 20$  Rayleighs right up to  $\sim 500$  Rayleighs. The curve in the trend beyond 500 Rayleighs is due to saturation effects with the SHS data. These points were discarded when making the calibration fit.

The reciprocal of the slope of the linear part of the relation provides a calibration factor of

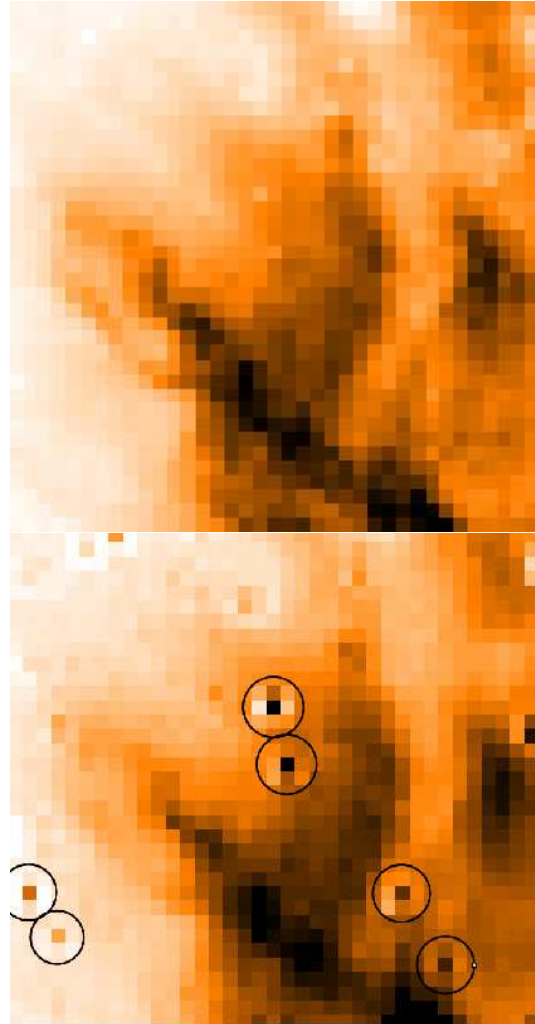


**Figure 14.** Two H $\alpha$  images of a 30' region of SHS field h350 centred on  $16^h 47^m - 49^\circ 00''$  (J2000) as in Figure 13. The top image is the SHS image blocked down to match the 48 arcsecond resolution of the SHASSA data and continuum subtracted. The bottom image is the equivalent SHASSA image, trimmed and aligned ready for comparison. Areas of uncanceled bright stars are highlighted

15.1 counts/pixel/Rayleigh to convert the SuperCOSMOS intensity counts to Rayleighs for this field. An estimate of the error in this calibration is possible, based on the vertical scatter of points about this trend, as a given SuperCOSMOS value matches a Rayleigh value in this vertical distribution. In this field the  $1\sigma$  scatter is 21 Rayleighs.

The data taken from the two areas in the SE corner of the SHS survey field required flat-field correction of up to 20 per cent. They behave very well when compared with the data requiring less correction, neatly overlaying the main trend, with no change in slope or increase in scatter. This

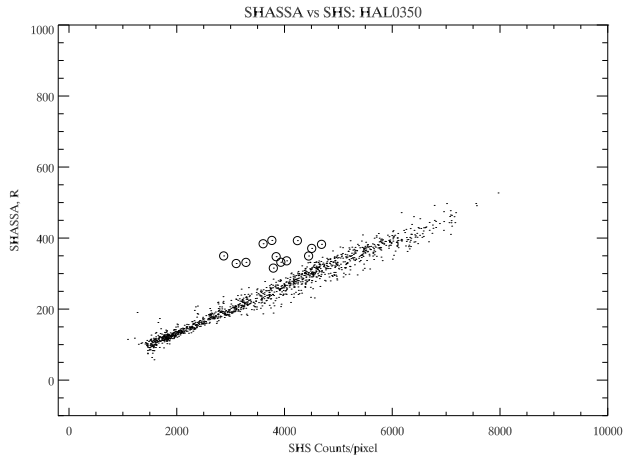


**Figure 15.** The comparison plot of SHS and SHASSA data from the area shown in Figure 14. Each point on the plot is the rebinned pixel value from the SHS data against the Rayleigh value from the SHASSA data. Note the linear relation and the large dynamic range covered by this comparison. The outliers due to uncanceled bright stars in the SHASSA data are highlighted.

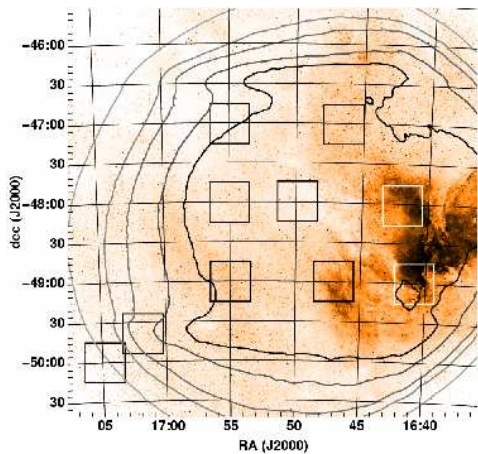


**Figure 16.** Blocked down image of survey field h350 with overlaid contours at 85, 90, 92, 95 and 97 per cent. The 30 arcminute areas used to make the comparison plot shown in Figure 17 are framed by the squares which are drawn in black or white to best contrast with their background. The bright HII region to the right is NGC 6188, excited by the young open cluster NGC 6193, nucleus of Ara OB 1.

justifies use of the data out to the 15 per cent flat-field contour where the emulsion records strong emission.

### 11.5 SHS sensitivity limit

While the results from field h350 have shown that the survey has been well tuned to the detection of diffuse emission, as well as giving an approximate limit to the point at which the photographic emulsion saturates, the faint limit has not yet

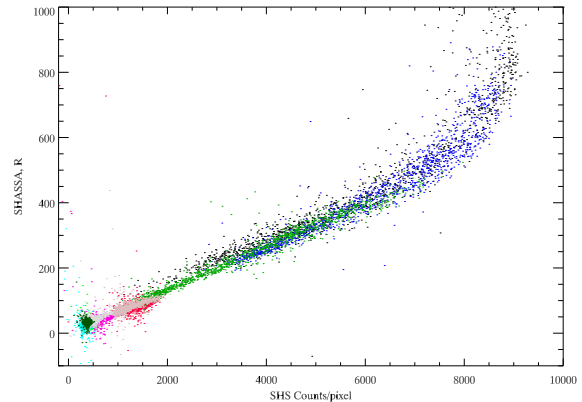


**Figure 17.** The comparison plot for all ten 30 arcminute areas highlighted in Figure 16. All align on the one trend, implying no variation in sensitivity across the SHS survey field. The bright photographic saturation is seen from  $\sim 500$  Rayleighs. The grey points at the faint end of the plot are taken from the area of poor filter response in the SE corner of h350 and align well with the rest of the data, indicating that, in areas of bright emission, flat-field corrections as large as 20 per cent still return reasonable intensity values.

been constrained because there is no really faint emission on this field. At the faintest point of 20 Rayleighs there is no sign of either survey struggling for sensitivity so a field exhibiting fainter emission is required to probe the SHS faint sensitivity limit. According to the SHASSA data an area of the Southern Galactic plane in Monoceros harbours diffuse emission that reaches a level as faint as  $\sim 2$  Rayleighs, which is ideal to test the faint limit of the SHS data. Figure 18 shows the 16 times blocked down  $H\alpha$  image of SHS field h1109, which covers this area of sky, with contours of filter response and the areas selected shown as with Figure 16. On this field, nine 30 arcminute regions have been examined as two groups: one, labelled 1–5 in Figure 18, from the area of best filter response and the other, labelled A–D, probing the combined effects of extremely low levels of emission and decreased filter transmission.

The comparison plot from the first group is shown in Figure 19. Once again, there is a clearly defined relation between the two, although on this faint field the upper saturation limit is not reached. It is immediately obvious that the SHS data can match the SHASSA data right down to the faintest level of emission, although the linear response of the SHS data is difficult to determine at this low level.



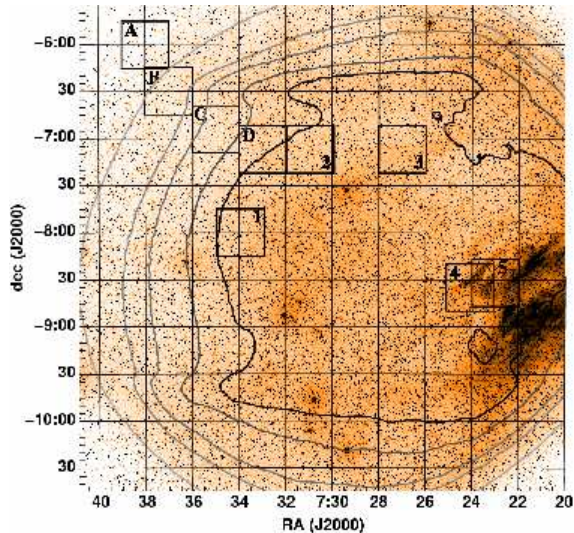


**Figure 18.** Blocked down SHS H $\alpha$  image of field h1109 with contours of filter response at 85, 90, 92, 95 and 97 per cent overlaid. Two groups of 30' areas are marked by squares and labelled to indicate group membership.

The SHS data are therefore detecting emission structure as faint as 2 Rayleighs on this field, although this sensitivity is tempered by the scatter evident in the plot and in the examination of the areas from the area of poor filter transmission discussed below. The linear fit returns a value of  $7.7 \pm 0.1$  SuperCOSMOS counts/pixel/Rayleigh for this particular field and provides a reasonable calibration as the  $1\sigma$  scatter to the fit is just 6.2 Rayleighs. Note the factor of two difference in the slope of the calibration curve for this low emission level field h1109 (no emission measure greater than about 80 Rayleighs seen in the area considered) compared to that obtained for high emission field h350 in Figure 17, which returned 15.1 counts/pixel/Rayleigh, which is closer to that generally obtained for most fields. This serves to emphasise the need for individual field calibration due to the variation in SuperCOSMOS pixel intensities on a given field, arising primarily from variable fog-level, sky background and resulting SuperCOSMOS and emulsion saturation.

### 11.6 Fifteen Fields Studied in Depth

A total of fifteen fields from a wide variety of Galactic environments were studied using several 30 arcminute regions in each in order to build up a global picture of the survey

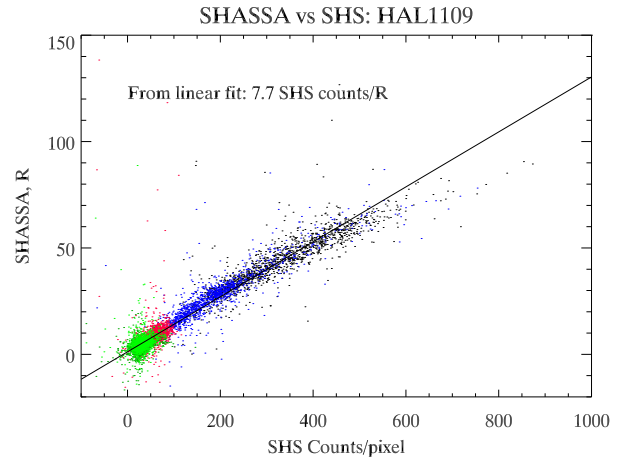


**Figure 19.** Calibration plot of the numbered 30 arcminute areas from the best area of filter response on field h1109. Points from each area are plotted as a different colour. Note the SHS data match the SHASSA data down to the faintest intensity at  $\sim 2$  Rayleighs. The linear fit is also plotted.

behaviour. The comparison plots for 4 of these are shown in Figure 20 with the linear fit overlaid. In each case a clear, essentially linear relation can be seen between the SHS and SHASSA data. Generally, different 30 arcminute regions follow a single trend which indicates little variation in emulsion sensitivity across the large SHS images. Three of the fields examined, h175, h350 and h555 show evidence for saturation at the bright end and fix the bright limit at  $\sim 500$  to  $\sim 600$  Rayleighs, while none of the fields appear to reach the background fog level in the areas that were compared.

### 11.7 Calibration of the entire SHS

From the analysis of the fifteen fields considered above, it is clear that each field requires individual calibration and that one, well selected, 30 arcminute area of SHS pixel data can be compared with SHASSA to give a working estimate of the calibration factor and a satisfactory result in most cases. On this basis, the 30 arcminute areas of pixel data which covered the greatest dynamic range of emission were downloaded from each of the 233 SHS fields, re-binned and compared with the equivalent area of SHASSA data. The results for each field can be found on the SHS web site. For each field the position of the area used, the computed scaling factor for continuum subtraction, the linear fit and, where

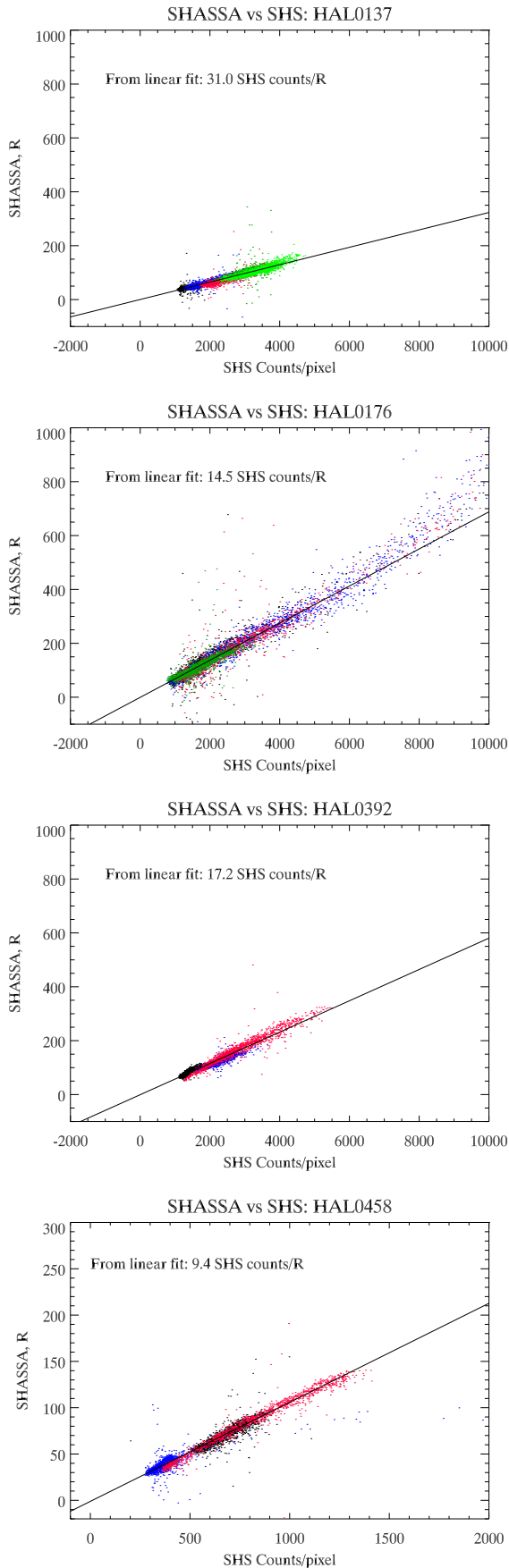


**Figure 20.** Comparison plots for four of the fifteen SHS fields

appropriate, the coefficients from a third-degree polynomial fit are given. The  $1\sigma$  vertical scatter about the linear fit is also quoted to offer an estimate of the error in the calibration. Of the 233 survey fields, 76 are relatively featureless and exhibit little emission. These are difficult to fit and in 9 cases the fit failed completely. Forty three of these show evidence of the low-level photographic fog. Of the remaining 157 fields, 122 are well constrained by a linear fit. For the other 35 fields the fit can be improved with a low-order polynomial relation. Where this is the case the coefficients are included in the table on the SHS website.

### 11.8 Calibration check of SHS field overlap regions

There is generous overlap between survey fields because of the circular aperture of the filter which allows field-to-field consistency check of the calibration. For six overlap regions between eight fields, a 30 arcminute area was carefully selected from the best possible compromise of filter response between two fields, never requiring flat-field correction greater than 15 per cent. The calibration factor calculated from the field centre in the best region of filter response was applied to these pixel data from the edge. For seven of the eight fields the calibration factor determined from the linear fit to the data was used. Calibrated and aligned data from the two overlapping SHS fields were plotted pixel by pixel at 0.67 arcsecond, 10 arcsecond and 48 arcsecond resolution. If the independently determined calibration applied to each field is consistent, the resulting plot of Rayleighs from one field against Rayleighs from its neighbour should yield a linear relation with slope of unity and no offset.

From the six fields examined in this way the results give good agreement. Four examples are shown in Figure 21 from comparisons at 48 arcsecond resolution. Here the ordinate and abscissa values are in Rayleighs with each axis labelled with its field. The fits are quoted on the plots and in Table 4. Two comparisons, 459-392 and 459-458, agree to better than 10 per cent, three more, 391-329, 458-391

and 460-459 also return linear results but agree to just 14, 29 and 43 per cent respectively. The bottom 3 comparisons are for overlapping fields so the good match implies that one could construct seamless, large pixel mosaics. For the h350 and h349 the linear relation is not so well behaved. The slightly curved trend between these two fields probably results from the bright saturation evident in the pixel data of the overlap region used (note the higher Rayleigh limits for this comparison).

## 12 COMPARISON WITH IPHAS

The SHS and IPHAS  $H\alpha$  surveys have areas of overlap at low declinations which permit a direct comparison to be made between the two complementary surveys. Figure 22 shows a  $3.3 \times 2$  arcminute region centred on  $18^h 47^m 42.6^s, +01^\circ 33' 04''$  which includes the newly discovered planetary nebula PHR1847+0132, taken from a slightly shallow SHS survey field h1332 (exposure number HA18088, survey grade A2, but exposure time cut short to 168mins cf. 180 normally). The data have been carefully matched in terms of co-ordinate projection but not otherwise processed. It is clear the two surveys achieve similar depth for diffuse emission but that the IPHAS survey goes deeper for point-sources due to its better resolution. Further details of the IPHAS survey are given by Drew et al. (2005).

## 13 COLOUR-COLOUR PHOTOMETRIC PLOTS

The SR,  $H\alpha$  ‘R-equivalent’ and  $I$  magnitudes can be combined to provide  $H\alpha - R$  and  $R - I$  colours for the objects detected by the IAM software. The narrowband  $H\alpha$  photometry should be sensitive to point-source emitters, so the SHS stellar photometry is of particular interest. A colour-magnitude diagram (CMD) of SR magnitude versus  $H\alpha - R$  can be constructed from the survey data to trace the average values of  $H\alpha - R$  for normal stars by brightness and help identify emitters by highlighting objects which stand apart

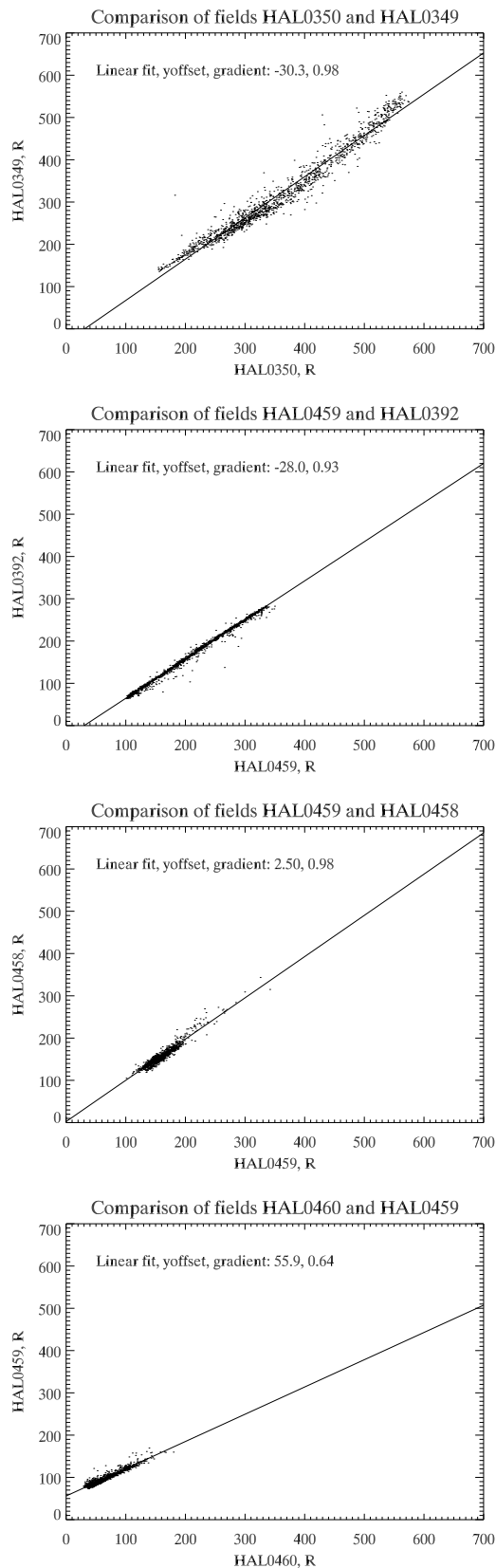
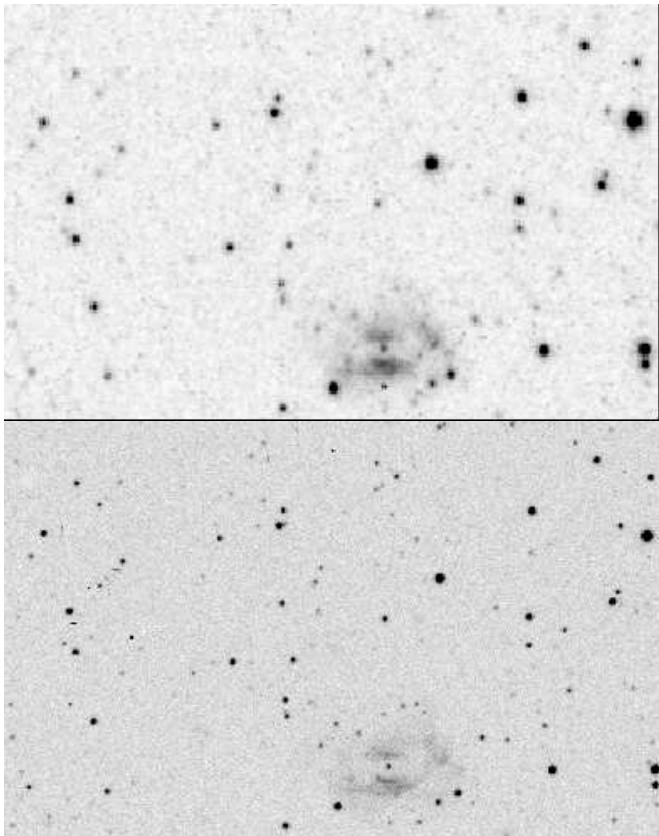


Figure 21. Comparisons between adjacent fields which have been calibrated according to a linear fit with SHASSA data.

**Table 4.** Fits obtained from the comparison of SuperCOSMOS pixel data in overlap regions between adjacent survey fields using linear calibration factors

Fields	Position	Slope	Slope10	Slope48	Calib1/Calib2
350 and 349	16 38 -48 00	0.88 <sup>a</sup>	0.95 <sup>a</sup>	0.97 <sup>a</sup>	1.03
391 and 329	08 25 -46 30	1.15	1.13	1.14	0.62
458 and 391	08 22 -42 15	0.49	0.54	0.57	1.44
459 and 392	08 48 -42 15	0.86	0.90	0.93	1.17
459 and 458	08 36 -40 30	0.90	0.91	0.89	0.93
460 and 459	08 56 -41 15	0.60	0.71	0.71	1.22

<sup>a</sup> This result is from a linear fit whereas a polynomial might be more appropriate. Refer to top panel in comparison plots given in Figure 21

**Figure 22.** A  $3.3 \times 2$  arcminute comparison region between SHS (top) and IPHAS (bottom) data centred on  $18^h47^m42.6^s, +01^\circ33'04''$  including the new planetary nebula PHR1847+0132.

from this. Figure 23a shows a CMD constructed from a  $1^\circ$  region from the centre of survey field h135. Most stars can be seen to congregate around a stellar locus running vertically in the diagram at  $H\alpha - R \sim -0.2$  and with an increasing spread towards fainter magnitudes. This is due to the census including a more complete population of objects at fainter magnitudes and increasing photon errors. Outliers can be

seen either side of the distribution and, if present, emission line objects will sit to the left of the main stellar locus.

A colour-colour plot of  $R - I$  vs  $H\alpha - R$  provides more information about the stellar population along a given line of sight. Figure 23b presents such a plot for the same area of sky as described above and uses the  $I$  band magnitudes which have been corrected to the SR photometry. In this plot the stellar locus is centred at  $H\alpha - R \sim -0.2$  and  $R - I = 0.15$ . The area covered suffers high reddening of up to  $E(B - V) = 4.7$  mag (Schlegel, Finkbeiner, & Davis, 1998) and this is evident in the stretching of the stellar locus towards larger values of  $R - I$  and, significantly,  $H\alpha - R$  making them appear to be emission line stars. These reddened non-emitters can be identified in the colour-colour plot of  $R - I$  versus  $H\alpha - R$  and excluded from studies of potential point-source emitters (Pierce 2005). An additional complication is the potential contamination from late type stars. A TiO opacity minimum near  $6536\text{\AA}$  enables the continuum to be attained, producing the peak, compared to the TiO band heads on either side of the  $H\alpha$  filter. Further to the red, the Tech-Pan emulsion sensitivity cuts off at  $6990\text{\AA}$ . Such objects can thus appear as apparent  $H\alpha$  emitters when compared to the matching SR photometry unless the complementary  $I$  band photometry is included, as such late type stars will be brighter in this band than  $H\alpha$  emitters. However, colour-colour plots created in 1-degree sub-regions, avoids the smearing effects on the photometry due to small positional shifts in the stellar locus across a  $H\alpha$  survey field. These have proved very effective in identifying

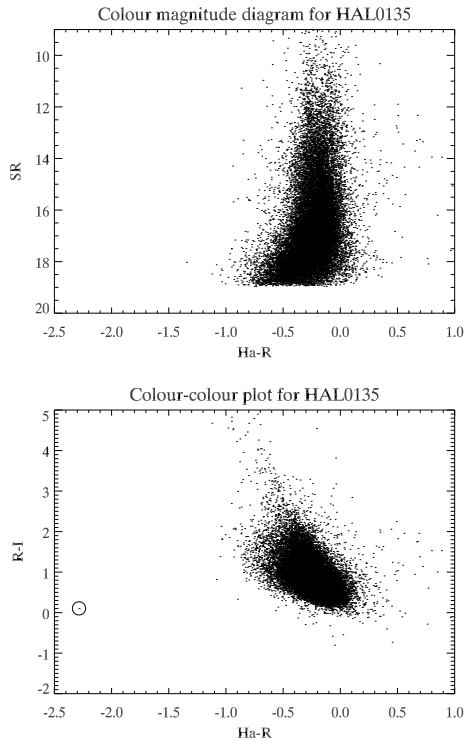


**Figure 23.** The colour magnitude diagram of  $SR$  vs  $H\alpha - R$  and the colour-colour plot of  $R - I$  vs  $H\alpha - R$  for stars from an area centred on the middle of SHS field h135. On average the stars sit at roughly neutral values of  $H\alpha - R = -0.2$  and  $R - I = 0.15$ . The reddening in this field of up to  $E(B-V) = 4.7$  mag is evident in the colour-colour plot as a smearing of the stellar locus towards higher values of  $R - I$  and  $H\alpha - R$ . The circled point indicates the location of a Planetary Nebulae.

point-source emission candidates and has been successfully employed to provide targets for follow-up multi-object spectroscopy with 6dF and 2dF at the AAO (e.g. Hopewell et al. 2005).

## 14 SCIENTIFIC EXPLOITATION

The SHS on-line atlas was released in stages starting in 2002 with the complete survey made available in 2003. A variety of programmes are underway to exploit the scientific potential of this new resource. Several illustrative project examples are briefly mentioned below.

### 14.1 Planetary Nebulae

The largest project arising from the AAO/UKST  $H\alpha$  survey has been the Macquarie/AAO/Strasbourg  $H\alpha$  planetary

nebula project (MASH; Parker et al. 2003, 2005 in preparation) which has uncovered about 1000 new Galactic planetary nebulae (PNe), nearly doubling the sample accrued from all sources over the last 100 years. Related projects concern identification of a significant new PNe population in the Galactic Bulge (e.g. Peyaud, Parker & Acker 2003) and the discovery of an important sample of Wolf-Rayet central stars of PNe (e.g. Morgan, Parker & Russeil 2001; Parker & Morgan 2003) including the detection of the only [WN] PN central star in the galaxy (Morgan, Parker & Cohen 2003). A possible new phase of PNe evolution has also been reported around a strongly masing OH-IR star (Cohen, Parker & Chapman 2005). A very large PN in an early stage of interaction with the ISM has also been discovered (Pierce et al. 2004) as well as two, very large bipolar PNe previously mis-identified as HII regions (Frew, Parker & Russeil 2005). A new sample of large ( $>4$  arcminute), highly evolved, low surface brightness PNe have also been found from examination of  $16 \times$  blocked down FITS images of the entire 233 fields of SHS survey. These blocked-down images effectively enhance large angular size low surface brightness features (e.g. Pierce et al. 2004; Frew & Parker 2005, in preparation). All these discoveries are being investigated with follow-up spectroscopy to determine the fundamental parameters of this significant new sample.

### 14.2 HII regions and regions of star formation

This type of study is currently ripe for exploitation with little work currently undertaken. Mader et al. (1999) report the discovery of a significant new population of Herbig-Haro objects from an SHS extension field in Orion and a large wind-blown bubble with secondary star-forming regions around its periphery by Cohen et al. (2002). Numerous very faint HII regions have also been discovered as a by-product of the MASH survey (Parker et al. in preparation). Many large features are evident including bubbles which trigger star-formation and induce velocity departures of the associated HII regions. Using data from the SHS and additional kin-

matic information from Fabry-Perot observations (Georgelin et al. 2000), the filamentary H $\alpha$  counterparts and triggered HII regions for the HI shell centered at 290.1+0.2 (Rizzo and Arnal, 1998) have been revealed. The high resolution of the data permits precise description of the morphology and extent of such HII regions. This is vital information in determining the location of the exciting stars which can be inferred via orientation of the observed rims and dust “elephant trunk” with respect to the HII region as a whole. Furthermore, the H $\alpha$  counterpart and visible extension can be directly compared to radio HII regions. This is essential information needed to determine the distance of HII regions in the framework of the study of the large scale structure of our Galaxy (Russeil et al., 2005).

### 14.3 Supernova Remnants

Several programmes searching for the optical counterparts of supernova remnants (SNRs) in the SHS have already been undertaken. Walker, Zealey & Parker (2001) report finding new filamentary shell structures traced by H $\alpha$  emission that are likely associated with Galactic SNRs. A more recent project is underway to uncover SNR candidates across the entire SHS from careful scrutiny of both the blocked-down FITS images and the original survey films, with several new SNRs already confirmed (Stupar, private communication). Searches for new optical H $\alpha$  counterparts around the known Galactic SNR overlapping the SHS is also underway. One new Galactic SNR discovered serendipitously via the MASH programme has already been reported (Parker, Frew & Stupar 2004). A significant increase in the known population of optically detected Galactic SNRs is promised.

### 14.4 Point-source emitters

One area of more recent study is the search for point-source emitters and the subsequent follow-up spectroscopy of candidates identified from the SHS H $\alpha$  and SR photometry. Drew et al (2004) report the discovery, via SHS photometry, of only the 4<sup>th</sup> known massive WO star in the Milky

Way Galaxy identified as part of a general programme of candidate point-source follow-up. Additionally, Hopewell et al. (2005) present five new WC9 stars discovered from the SHS data in a similar fashion. Pierce (2005) and Pierce et al. (2005, in preparation) demonstrate the power of the SHS to reveal significant new populations of H $\alpha$  emitters via a particular study in the Vela molecular ridge, especially when combined with *I* band and 2MASS photometry. These preliminary projects have been finding, for the magnitude range explored most thoroughly ( $12 < R < 16.5$ ), that 10-20 per cent of candidates are confirmed as emission line objects via follow-up spectroscopy. Their H $\alpha$  equivalent widths usually exceed 20Å. More recent work by Pierce (2005) indicates that the situation can be improved by weeding out M stars more thoroughly using the 2MASS data.

## 15 CONCLUSIONS

The AAO/UKST H $\alpha$  survey as scanned by SuperCOSMOS is now complete and on-line as the SHS atlas. It represents a powerful tool for the study of the ionized gas content of our galaxy on a range of spatial scales from arcsecond to tens of degrees. The distribution and structure of the ionised gas result from a wide range of astrophysically interesting phenomena. The astrometric and photometric properties have been described and shown to be well behaved and adequate for most purposes. Importantly, despite difficulties associated with photographic data and the scanning process, comparison with the independently calibrated SHASSA images has shown that the SHS survey faithfully records diffuse Galactic emission over a wide range of intensities from  $\sim 5$  Rayleighs to 500 Rayleighs. Emission down to  $\sim 2$  Rayleighs has been detected on one field, h1109. A calibration scheme for all 233 survey fields has been generated, based on comparison of a carefully selected, 30 arcminute region from each field with the equivalent area of intensity calibrated SHASSA H $\alpha$  image. If the limitations of the data are respected in terms of dynamic range, reliable flux estimates are possible. The survey is clearly appropriate for studies

of individual H $\alpha$  emitting objects including point-sources as well as being suitable for the study of the ionized interstellar medium in general. A variety of projects exploiting this resource are already underway and many exciting discoveries have already been made. The community is invited to consider use of this valuable survey when undertaking any study of the Southern Galactic Plane.

### ACKNOWLEDGEMENTS

The authors gratefully acknowledge the support of the AAO board, the Wide-Field Astronomy Unit at the University of Edinburgh, the Wide-Field Astronomy Panel (UK), the Particle-Physics and Astronomy Research Council and the AAO directors Russell Cannon and Brian Boyle and UKST astronomers-in-charge Ann Savage and Fred Watson for making the SHS survey possible. This paper used comparison data from SHASSA which was produced with support from the National Science Foundation. MC thanks NASA for supporting his participation in the SHS through LTSA grant NAG5-7936 with UC Berkeley. MJP thanks PPARC for provision of a PhD studentship. We also thank the referee John Meaburn for valuable comments on this paper.

### REFERENCES

Arrowsmith P., & Parker Q.A., 2001, ROE internal report  
 Beard S.M., MacGillivray H.T., Thanisch P.F., 1990, MNRAS, 247, 311  
 Bland-Hawthorn J.B., Veilleux S., Cecil G.N., Putman M.E., Gibson B.K., Maloney P.R., 1998, MNRAS, 299, 611  
 Bok B.J., Bester, M.J., Wade, C.M., 1955, Daedalus, 86, 9  
 Bond I.A. et al., 2001, MNRAS, 327, 868  
 Boyle B.J., Shanks T., Croom S.M., 1995, MNRAS, 276, 33  
 Buxton M. et al., 1998, PASA, 15, 24  
 Cohen M., Green A., Parker Q.A., Mader S., Cannon R.D. 2002, MNRAS, 336, 736  
 Cohen M., Parker, Q.A., Chapman, J., 2005, MNRAS, 357, 1189

Croom S.M., Ratcliffe A., Parker, Q.A., Shanks T., Boyle, B.J., Smith R.J., 1999, MNRAS, 306, 592  
 Davies R.D., Elliott K.H., Meaburn J., 1976, Mem. RAS, 81, 89  
 Dennison B., et al., 1998, PASA, 15, 147  
 Dopita M.A., Hua C.T., 1997, ApJS, 108, 515  
 Dopita M.A., Mathewson D.S., Ford V.L., 1985, ApJ, 297, 599  
 Drew J., Barlow M.J., Unruh Y.C., Parker Q.A., Wesson R., Pierce M.J., Masheder M.R.W., Phillipps S., 2004, MNRAS, 351, 206  
 Drew J. et al., 2005, MNRAS, submitted  
 Elliot K.H., Meaburn J., 1976, Ap&SS, 39, 437  
 Elmegreen B., Lada C.J., 1977, ApJ, 214, 725  
 Finkbeiner D.P., 2003, ApJS, 146, 407  
 Frew D.J., Parker Q.A., Russeil D., 2005, MNRAS, submitted  
 Gaustad J.E., McCullough P.R., Rosing W., & Van Buren D., 2001, PASP, 113, 1326  
 Georgelin Y.P., Georgelin Y.M., 1970, A&AS, 3, 1  
 Georgelin Y.M., Russeil D., Amram P. et al., 2000, A&A, 357,c308  
 Gerola H., Seiden P., 1978, ApJ, 223, 129  
 Green A.J., Cram L.E., Large M.I., Ye T., 1999, ApJS, 122, 207  
 Gum C.S., 1952, Observatory, 72, 151  
 Gum C.S., 1955, Mem.RAS, 67, 155  
 Haffner L.M., Reynolds R.J., Tufte S.L., Madsen G.J., Jaehnig K.P., Percival J.W., 2003, ApJS, 149, 405  
 Hambly N.C., Miller L., MacGillivray H.T., Herd J.T., Cormack W.A., 1998, MNRAS, 298, 897  
 Hambly N.C., et al., 2001a, MNRAS, 326, 1279  
 Hambly N.C., Irwin M.J., MacGillivray H.T., 2001b, MNRAS, 326, 1295  
 Hambly N.C., Davenhall A.C., Irwin M.J., MacGillivray H.T., 2001c, MNRAS, 326, 1315  
 Hase V.F., Shajn G.A., 1955, Isv. Krym. Astrofiz. Obs., 15, 11  
 Hog E., Fabricius C., Makarov V.V., Urban S., Corbin T.,

- Wycoff G., Bastian U., Schwekendiek P., Wicenec A., 2000, *A&A*, 355, L27
- Hopewell E. C., Barlow M. J., Drew J. E., Unruh Y. C., Pierce M. J., Parker Q. A., Knigge C., Phillipps S., Zijlstra A. A., 2005, *MNRAS*, submitted.
- Jarrett T., Chester T., Cutri R., Schneider S., Skrutskie M., Huchra J.P., 2000, *AJ*, 119, 2498
- Johnson H.M., 1955, *ApJ*, 121, 604
- Johnson H.M., 1956, *ApJ*, 124, 90
- Keller S.C., Grebel E.K., Miller G.J., Yoss K.M., 2001, *AJ*, 122, 248
- Kennicutt R.C., 1992, *ApJ*, 388, 310
- Kodak publication P-315, 1987, Scientific imaging with Kodak films and plates
- Lasker B.M., et al., 1988, *ApJS*, 68, 1
- Mader S.L., Zealey W.J., Parker Q.A., Masheder M.R.W., 1999, *MNRAS*, 310, 331
- Meaburn J., 1978, *Applied Optics*, 17, 1271
- Meaburn J., 1980, *MNRAS*, 192, 365
- Meaburn J., White N.J., 1982, *MNRAS*, 200, 771
- Mel'Nik A.M., Efremov Y.N., 1995, *AstL*, 21, 10
- Miller L., Cormack W.A., Paterson M.G., Beard S.M., Lawrence L., 1992, In MacGillivray H.T., Thomson E.B., eds, *Digitised Optical Sky Surveys*, Kluwer, Dordrecht, p.133
- Morgan D.H., Parker Q.A., & Russeil D., 2001, *MNRAS*, 322, 877.
- Morgan D.H., Parker Q.A., Cohen M., 2003, *MNRAS*, 346, 729
- Morgan D.H., Parker Q.A., 2005, *MNRAS*, in press
- Nossal S., et al., 2001, *J.Geophys.Res.* 5605
- Osterbrock D.E., 1989, *Astrophysics of Gaseous Nebulae*, University Science Books
- Parker Q.A., Bland-Hawthorn J., 1998, *PASA*, 15, 33
- Parker Q.A., Malin D.F., 1999, *PASA*, 16, 288
- Parker Q.A., Phillipps S., 1997, *PASA*, 15, 28
- Parker Q.A., Phillipps S., 1998, *A&G*, 39, 4.10
- Parker Q.A., Phillipps S., 2003, in *ASP Conf.Ser.* 289: Proceedings of the IAU 8th Asian-Pacific Regional Meeting, Volume I, 165
- Parker Q.A., Hartley M., Russeil D., Acker A., Ochsenbein F., Morgan D.H., Beaulieu S., Morris R., Phillipps S., Cohen, M., 2003, *ASP Conf.Ser.* eds M.Dopita, S.Kwok and R Sutherland, p.41
- Parker Q.A., Morgan D.H., 2003, *MNRAS*, 341, 961
- Parker Q.A., Frew D.J., Stupar M., 2004, *AAO Newsletter*, 104, 9
- Peyaud A.E.J., Parker Q.A., Acker A., 2003, in *SF2A-2003: Semaine de l'Astrophysique Francaise*, 311
- Phillipps S., Parker Q.A., 1993, *MNRAS*, 265, 385
- Pickering W.H., 1890, *Sidereal Messenger*, 9, 2
- Pierce M.J., Frew D.J., Parker Q.A., Koppen J., 2004, *PASA*, 21, 334
- Pierce, M., 2005, PhD thesis, University of Bristol
- Price S.D., Egan M.P., Carey S.J., Mizuno D., Kuchar T. 2001, *AJ*, 121, 2819
- Rizzo J.R., Arnal E.M., 1998, *A&A* 332, 1025
- Rodgers A.W., Campbell C.T., Whiteoak J.B., 1960, *MNRAS*, 121, 103
- Russeil D., et al., 1997, *A&A*, 319, 788
- Russeil D., et al., 1998, *PASA*, 15, 9
- Russeil D., Adami C., Amram P., Coarer E., Georgelin T.M., Marcelin M., Parker Q.A., 2005, *A&A*, 429, 497
- Schlegel D.J., Finkbeiner D.P., Davis M., 1998, *ApJ*, 500, 525
- Sharpless S., 1953, *ApJ*, 118, 362
- Sharpless S., 1959, *ApJS*, 4, 257
- Sivan, 1974, *A&A*, 16, 163
- Stephenson C.B., & Sanduleak N., 1977, *ApJS*, 33, 459
- Storkey A.J., Hambly N.C., Williams C.K.I., Mann R.G., 2004, *MNRAS*, 347, 36
- Sung H., Chun M., Bessell M.S., 2000, *AJ*, 120, 333
- Tenorio-Tagle G., Palous J., 1987, *A&A*, 186, 287
- Tritton S.B., 1993, *UKSTU Handbook*, publication of the Royal Observatory Edinburgh
- Walker A., Zealey W.J., Parker Q.A., 2001, *PASA*, 18, 259
- Watson F.G. 1984, *MNRAS*, 206, 661



Zacharias N., Urban S.E., Zacharias M.I., Wycoff G.L., Hall

D.M., Monet D.G., Raffert T.J., 2004, AJ, 127,3043